



The Detection of [O III] λ 4363 in a Lensed, Dwarf Galaxy at $z = 2.59$: Testing Metallicity Indicators and Scaling Relations at High Redshift and Low Mass*

Timothy Gburek¹ , Brian Siana¹ , Anahita Alavi^{1,2} , Najmeh Emami¹ , Johan Richard³ , William R. Freeman¹ , Daniel P. Stark⁴, Christopher Snapp-Kolas¹, and Breanna Lucero¹

¹ Department of Physics & Astronomy, University of California, Riverside, CA 92521, USA; timothy.gburek@email.ucr.edu

² Infrared Processing and Analysis Center, Caltech, Pasadena, CA 91125, USA

³ Univ Lyon, Univ Lyon1, Ens de Lyon, CNRS, Centre de Recherche Astrophysique de Lyon UMR5574, F-69230, Saint-Genis-Laval, France

⁴ Department of Astronomy, Steward Observatory, University of Arizona, 933 North Cherry Avenue, Rm N204, Tucson, AZ 85721, USA

Received 2019 June 27; revised 2019 November 4; accepted 2019 November 11; published 2019 December 18

Abstract

We present Keck/MOSFIRE (Multi-Object Spectrometer for InfraRed Exploration) and Keck/LRIS (Low Resolution Imaging Spectrometer) spectroscopy of A1689-217, a lensed (magnification ~ 7.9), star-forming (SFR $\sim 16 M_{\odot} \text{ yr}^{-1}$), dwarf ($\log(M_*/M_{\odot}) = 8.07\text{--}8.59$) Ly α emitter ($EW_0 \sim 138 \text{ \AA}$) at $z = 2.5918$. Dwarf galaxies similar to A1689-217 are common at high redshift and likely responsible for reionization, yet few have been studied with detailed spectroscopy. We report a 4.2σ detection of the electron-temperature-sensitive [O III] λ 4363 emission line and use this line to directly measure an oxygen abundance of $12 + \log(\text{O}/\text{H}) = 8.06 \pm 0.12$ ($\sim 1/4 Z_{\odot}$). A1689-217 is the lowest-mass galaxy at $z > 2$ with an [O III] λ 4363 detection. Using the rest-optical emission lines, we measure A1689-217's other nebular conditions, including electron temperature ($T_e([\text{O III}]) \sim 14,000 \text{ K}$), electron density ($n_e \sim 220 \text{ cm}^{-3}$), and reddening ($E(B - V) \sim 0.39$). We study relations between strong-line ratios and direct metallicities with A1689-217 and other galaxies with [O III] λ 4363 detections at $z \sim 0\text{--}3.1$, showing that the locally calibrated, oxygen-based, strong-line relations are consistent from $z \sim 0$ to 3.1. We also show additional evidence that the O_{32} versus R_{23} excitation diagram can be utilized as a redshift-invariant, direct-metallicity-based, oxygen abundance diagnostic out to $z \sim 3.1$. From this excitation diagram and the strong-line ratio–metallicity plots, we observe that the ionization parameter at fixed O/H is consistent with no redshift evolution. Although A1689-217 is metal-rich for its M_* and star formation rate, we find it to be consistent within the large scatter of the low-mass end of the fundamental metallicity relation.

Unified Astronomy Thesaurus concepts: Galaxy abundances (574); Dwarf galaxies (416); Galaxy evolution (594); High-redshift galaxies (734); Interstellar medium (847)

1. Introduction

Gas-phase metallicity, measured as nebular oxygen abundance, is a fundamental property of galaxies and is critical to understanding how they evolve across cosmic time. Metallicity traces the complex interplay between heavy-element production via star formation/stellar nucleosynthesis and galactic gas flows, whereby infalling gas dilutes the interstellar medium (ISM) with metal-poor gas, and outflowing gas removes metals from the galaxy. These gas flows also relate to star formation and feedback, in which cold gas falls into the galaxy, triggering star formation that is later quenched by enriched outflows from supernovae that heat the ISM and remove the gas needed for star formation. As a tracer of the history of inflows and outflows, metallicity measurements at different redshifts constrain the timing and efficiency of processes responsible for galaxy growth.

This connection between metallicity and the buildup of stellar mass is encapsulated in the stellar mass (M_*)–gas-phase

metallicity (Z) relation (MZR) of star-forming galaxies, seen both locally (e.g., Tremonti et al. 2004; Kewley & Ellison 2008; Andrews & Martini 2013) and at high redshift (e.g., Erb et al. 2006; Maiolino et al. 2008; Henry et al. 2013; Zahid et al. 2013; Steidel et al. 2014; Sanders et al. 2015, 2019), where metallicities are lower at fixed stellar mass. The relation shows that low-mass galaxies are more metal-poor than their high-mass counterparts, possibly due to the increased effectiveness of galactic outflows (feedback) in shallower potential wells. Constraining the MZR and its redshift evolution is vital to constraining the processes ultimately responsible for galaxy formation and evolution.

The mass–metallicity relation has also been shown to derive from a more general relation between stellar mass, star formation rate (SFR), and oxygen abundance. This M_* –SFR– Z connection, the fundamental metallicity relation (FMR), was first shown to exist by Mannucci et al. (2010) with $\sim 140,000$ Sloan Digital Sky Survey (SDSS; Abazajian et al. 2009) galaxies, and independently by Lara-López et al. (2010) with $\sim 33,000$ SDSS galaxies. The FMR constitutes a 3D surface with these three properties, for which metallicity is tightly dependent on stellar mass and SFR with a residual scatter of ~ 0.05 dex (Mannucci et al. 2010), a reduction in the scatter observed in the MZR. The FMR is also observed to be redshift invariant out to $z = 2.5$ (Mannucci et al. 2010; see also sources within the review of Maiolino & Mannucci 2019), suggesting that the observed evolution of the MZR over this redshift range is the result of observing different parts of the locally defined

* The data presented herein were obtained at the W. M. Keck Observatory, which is operated as a scientific partnership among the California Institute of Technology, the University of California, and the National Aeronautics and Space Administration. The Observatory was made possible by the generous financial support of the W. M. Keck Foundation. Based on observations made with the NASA/ESA Hubble Space Telescope, obtained from the Data Archive at the Space Telescope Science Institute, which is operated by the Association of Universities for Research in Astronomy, Inc., under NASA contract NAS5-26555. These observations are associated with programs #9289, #11710, #11802, #12201, #12931.

FMR at different redshifts. Above $z = 2.5$, galaxies have lower metallicities than predicted by the locally defined FMR (Mannucci et al. 2010; Troncoso et al. 2014; Onodera et al. 2016). These studies analyze galaxies at $z \gtrsim 3$, where the strong optical emission lines used for metallicity determination are again observable in the H band and K band.

To accurately constrain the evolution of the MZR and FMR across redshift, metallicities must be estimated via a method that is consistent at all redshifts. Ideally, this is accomplished through first measuring other intrinsic nebular properties that dictate the strength of the collisionally excited emission lines necessary for oxygen abundance determination. This “direct” method estimates the electron temperature (T_e) and density (n_e) of nebular gas, in conjunction with flux ratios of strong oxygen lines to Balmer lines, to determine the total oxygen abundance (e.g., Izotov et al. 2006). Electron temperature is calculated via a temperature-sensitive ratio of strong emission lines, commonly [O III] $\lambda 5007$, to auroral emission lines, such as [O III] $\lambda 4363$ or [O III] $\lambda \lambda 1661, 1666$, from the same ionic species. The [O III] $\lambda 4363$ line and flux ratio of [O III] $\lambda \lambda 4959, 5007$ /[O III] $\lambda 4363$ are preferred, as all lines lie in the rest-optical part of the electromagnetic spectrum. However, the [O III] $\lambda 4363$ line is faint, ~ 40 – 100 times weaker than [O III] $\lambda 5007$ in low, subsolar-metallicity galaxies, and still weaker in higher-metallicity sources, where metal cooling is more efficient. This makes observing the line difficult locally, and especially difficult at high redshift. Only 11 galaxies at $z > 1$ have been detected (most via gravitational lensing) with significant [O III] $\lambda 4363$ (Yuan & Kewley 2009; Brammer et al. 2012; Christensen et al. 2012; Stark et al. 2013; James et al. 2014; Maseda et al. 2014; Sanders et al. 2016b, 2019), and of those, only 3 are at $z > 2$ (Sanders et al. 2016b, 2019).

In an effort to circumvent this problem and extend our ability to measure oxygen abundance to both high-metallicity and high-redshift galaxies, “strong-line” methods were developed to estimate abundances via flux ratios of strong, nebular emission lines (e.g., Jensen et al. 1976; Alloin et al. 1979; Pagel et al. 1979; Storchi-Bergmann et al. 1994). These indirect methods utilize calibrations of the correlations between these strong-line ratios and metallicities derived empirically with direct-metallicity measurements of nearby H II regions and galaxies (e.g., Pettini & Pagel 2004; Pilyugin & Thuan 2005), theoretically with photoionization models (e.g., McGaugh 1991; Kewley & Dopita 2002; Dopita et al. 2013), or with a combination of both (e.g., Denicoló et al. 2002). However, as almost all of these calibrations have been done locally owing to the inherent observational difficulties of the T_e -based, direct method (see Jones et al. 2015 for the first calibrations done at an appreciable redshift, $z \sim 0.8$), the question has naturally arisen as to whether these calibrations are accurate at high redshift.

With the statistical spectroscopic samples of high-redshift galaxies that now exist, there is evidence that physical properties of high- z , star-forming regions are different than what are observed locally. This is typically shown with the well-known offset of the locus of star-forming, high-redshift galaxies relative to that of local, star-forming SDSS galaxies in the [O III] $\lambda 5007$ /H β versus [N II] $\lambda 6583$ /H α Baldwin–Phillips–Terlevich (N2-BPT; Baldwin et al. 1981) diagnostic diagram (Steidel et al. 2014; Shapley et al. 2015; Sanders et al. 2016a; Kashino et al. 2017; Strom et al. 2017). Numerous studies have tried to explain the primary cause of this

evolution, with various conclusions. It has been suggested that the offset derives from an elevated ionization parameter (Brinchmann et al. 2008; Cullen et al. 2016; Hirschmann et al. 2017; Kashino et al. 2017), elevated electron density (Shirazi et al. 2014), harder stellar ionizing radiation (Steidel et al. 2014; Strom et al. 2017, 2018), and/or an increased N/O abundance ratio in high- z galaxies (Masters et al. 2014; Shapley et al. 2015; Sanders et al. 2016a). It is also possible that there is no single primary cause and the offset is due to a combination of the aforementioned property evolutions (Kewley et al. 2013; Maiolino & Mannucci 2019). Nevertheless, there is considerable motivation to check the validity of locally calibrated, strong-line metallicity methods at high redshift that utilize the emission lines in the N2-BPT plot and emission lines of other diagnostic diagrams, such as the S2-BPT variant ([O III] $\lambda 5007$ /H β vs. [S II] $\lambda \lambda 6716, 6731$ /H α) and the O $_{32}$ versus R $_{23}$ (see Equations (2) and (3), respectively) excitation diagram.

In this paper, we present a detection of the auroral [O III] $\lambda 4363$ emission line in a low-mass, lensed galaxy (A1689-217) at $z = 2.59$. We determine the direct metallicity of A1689-217 and combine it with other (recalculated) direct-metallicity estimates from the literature to examine the applicability of locally calibrated, oxygen- and hydrogen-based, strong-line metallicity relations at high redshift. In Section 2 we give an overview of the spectroscopic and photometric observations of A1689-217 and their subsequent reduction. Section 3 discusses the emission-line spectrum of A1689-217, highlighting the detection of [O III] $\lambda 4363$ and the method with which the spectrum was fit. Section 4 examines the physical properties of A1689-217 calculated from the photometry and spectroscopy. Section 5 discusses the results of the paper, focusing on the validity and evolution of strong-line metallicity relations with redshift, the evolution of ionization parameter with redshift, the position of A1689-217 in relation to the low-mass end of the FMR, and the position of A1689-217 relative to the predicted MZR from the Feedback In Realistic Environments (FIRE) hydrodynamical simulations. Section 6 gives a summary of our results. The Appendix revisits the [O III] $\lambda 4363$ detection of Yuan & Kewley (2009) with a more sensitive spectrum of the galaxy, taken as part of our larger, dwarf galaxy survey. Throughout this paper, we assume a Λ CDM cosmology, with $H_0 = 70 \text{ km s}^{-1} \text{ Mpc}^{-1}$, $\Omega_\Lambda = 0.7$, and $\Omega_m = 0.3$.

2. Observations and Data Reduction

In this section, we discuss the spectroscopic and photometric observations and reduction for A1689-217, lensed by the foreground galaxy cluster A1689. A1689-217 was initially detected via Lyman break dropout selection in the *Hubble Space Telescope* (*HST*) survey of Alavi et al. (2014, 2016). Based on its photometric redshift and high magnification ($\mu = 7.89$), it was selected for spectroscopic observation of its rest-frame optical, nebular emission lines as part of a larger spectroscopic survey of star-forming, lensed, dwarf galaxies.

2.1. Near-IR Spectroscopic Data

Near-IR (rest-optical) spectroscopic data for A1689-217 were taken on 2014 January 2 and 2015 January 17 with the Multi-Object Spectrometer for InfraRed Exploration (MOS-FIRE; McLean et al. 2010, 2012) on the 10 m Keck I telescope. Spectroscopy was taken in the J , H , and K bands with H -band

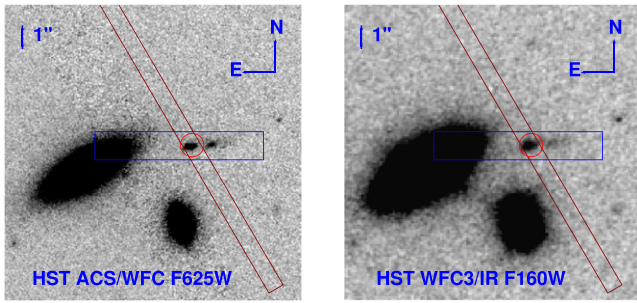


Figure 1. *HST* images of A1689-217 in the ACS/WFC F625W band and WFC3/IR F160W band. The $0''.7$ MOSFIRE slit is shown in light brown, and the $1''.2$ LRIS slit is shown in blue. A1689-217 is highlighted by the red circle. Foreground galaxies lie to the south and east of A1689-217. Both images are $12''.64$ on each side.

and *K*-band data taken the first night (2014) and data in all three bands taken the second night (2015). *J*-band and *H*-band data consist of 120 s individual exposures, while 180 s exposures were used in the *K* band. In total, the integration time is 80 minutes in *J* band, 104 minutes in *H* band (56 minutes in 2014 and 48 minutes in 2015), and 84 minutes in *K* band (60 minutes in 2014 and 24 minutes in 2015). The data were taken with a $0''.7$ -wide slit (see orientation in Figure 1), giving spectral resolutions of $R \sim 3310$, 3660, and 3620 in the *J*, *H*, and *K* bands, respectively. An ABBA dither pattern was utilized for all three filters, with $1''.25$ nods for the *J* band and $1''.2$ nods for the *H* and *K* bands.

The spectroscopic data were reduced with the MOSFIRE Data Reduction Pipeline⁵ (DRP). This DRP outputs 2D flat-fielded, wavelength-calibrated, background-subtracted, and rectified spectra combined at each nod position. Night-sky lines are used to wavelength-calibrate the *J* and *H* bands, while a combination of sky lines and a neon arc lamp is used for the *K* band. The 1D spectra were extracted using the IDL software BMEP⁶ from Freeman et al. (2019). The flux calibration of the spectra was first done with a standard star that was observed at an air mass similar to that of the A1689-217 observations, and then an absolute flux calibration was done using a star included in the observed slit mask.

2.2. Optical Spectroscopy

A deep optical (rest-frame UV) spectrum of A1689-217 was taken with the Low Resolution Imaging Spectrometer (LRIS; Oke et al. 1995; Steidel et al. 2004) on Keck I on 2012 February 24 with an exposure time of 210 minutes. The slit width was $1''.2$, and the slit was oriented E–W, as seen in Figure 1. We used the 400 line mm^{-1} grism, blazed at 3400 Å, on the blue side. To reduce read noise, the pixels were binned by a factor of two in the spectral direction. The resulting resolution is $R \sim 715$. The individual exposures were rectified, cleaned of cosmic rays, and stacked using the pipeline of Kelson (2003).

2.3. Near-UV, Optical, and Near-IR Photometry

Near-UV images of the A1689 cluster, all of them covering A1689-217, were taken with the Wide Field Camera 3 (WFC3)/UVIS channel on the *HST*. We obtained 30 orbits

in the F275W filter and 4 orbits in F336W with program ID 12201, followed by 10 orbits in F225W and an additional 14 orbits in F336W (18 orbits total) with program ID 12931. The data were reduced and photometry was measured as described in Alavi et al. (2014, 2016).

In the optical, we used existing *HST* Advanced Camera for Surveys (ACS)/WFC images in the F475W, F625W, F775W, and F850LP filters (PID: 9289; PI: H. Ford), as well as in the F814W filter (PID: 11710; PI: J. Blakeslee), calibrated and reduced as detailed in Alavi et al. (2014). The number of orbits and the 5σ depths measured within a $0''.2$ radius aperture for all optical and near-UV filters are given in Alavi et al. (2016, Table 1). In the near-IR, we used existing WFC3/IR images in the F125W and F160W filters (PID: 11802; PI: H. Ford), both with 2512 s exposure times.

Images of A1689-217 in the optical F625W filter and near-IR F160W filter are shown in Figure 1.

3. Emission-line Spectrum of A1689-217

The MOSFIRE spectra yield several emission lines necessary for the direct measurement of intrinsic nebular properties of A1689-217, located at $z = 2.5918$ (see Section 3.2). Seen in both 1D and 2D in Figure 2, we strongly detect [O II] $\lambda\lambda 3726, 3729$, $H\gamma$, $H\beta$, [O III] $\lambda 4959$, and $H\alpha$. We also detect the auroral [O III] $\lambda 4363$ line in the *H* band (discussed in greater detail in Section 3.1). The [O III] $\lambda 5007$ emission line, necessary for electron temperature (T_e) measurements, is not shown in Figure 2 because it sits at the edge of the *H*-band filter, where transmission declines rapidly, and the flux calibration is uncertain. We instead scale up from the [O III] $\lambda 4959$ line flux using the T_e -insensitive intrinsic flux ratio of the doublet, [O III] $\lambda 5007$ /[O III] $\lambda 4959 = 2.98$ (Storey & Zeippen 2000). We also note the lack of a significant detection of the [N II] $\lambda\lambda 6548, 6583$ doublet in this spectrum, placing A1689-217 in the upper left corner of the N2-BPT diagnostic diagram as seen in Figure 3. We conclude that A1689-217 is not an active galactic nucleus (AGN) based on its very low [N II]/ $H\alpha$ ratio, lack of high-ionization emission lines like [Ne V], and narrow line widths ($\sigma_{H\beta} \approx 53 \text{ km s}^{-1}$). The optical spectrum shows strong $\text{Ly}\alpha$ emission (see Figure 4) with a rest-frame equivalent width of $\text{EW}_{0,\text{Ly}\alpha} = 138 \text{ \AA}$, redshifted by 282 km s^{-1} . The slit-loss-corrected, observed emission-line fluxes and uncertainties are given in Table 1, with the line-fitting technique described in Section 3.2.

3.1. Detection of [O III] $\lambda 4363$

We report a 4.2σ detection of the T_e -sensitive, auroral [O III] $\lambda 4363$ line. In Figure 2, there is visible emission in the 2D spectrum at the observed wavelength and spatial coordinates expected for the emission line (as well as the expected symmetric negative images on either side resulting from nodding along the slit). In the magnified inset plot of the highlighted region of the 1D spectrum, there is a clear peak centered at the observed wavelength expected for [O III] $\lambda 4363$ at $z = 2.5918$. We note that this peak is part of 4 consecutive pixels that have a signal-to-noise ratio (S/N) > 1 . We also note that at A1689-217's redshift the [O III] $\lambda 4363$ line is not subject to sky-line contamination and thus conclude that this detection is robust.

⁵ <https://keck-datareductionpipelines.github.io/MosfireDRP/>

⁶ <https://github.com/billfreeman44/bmep>

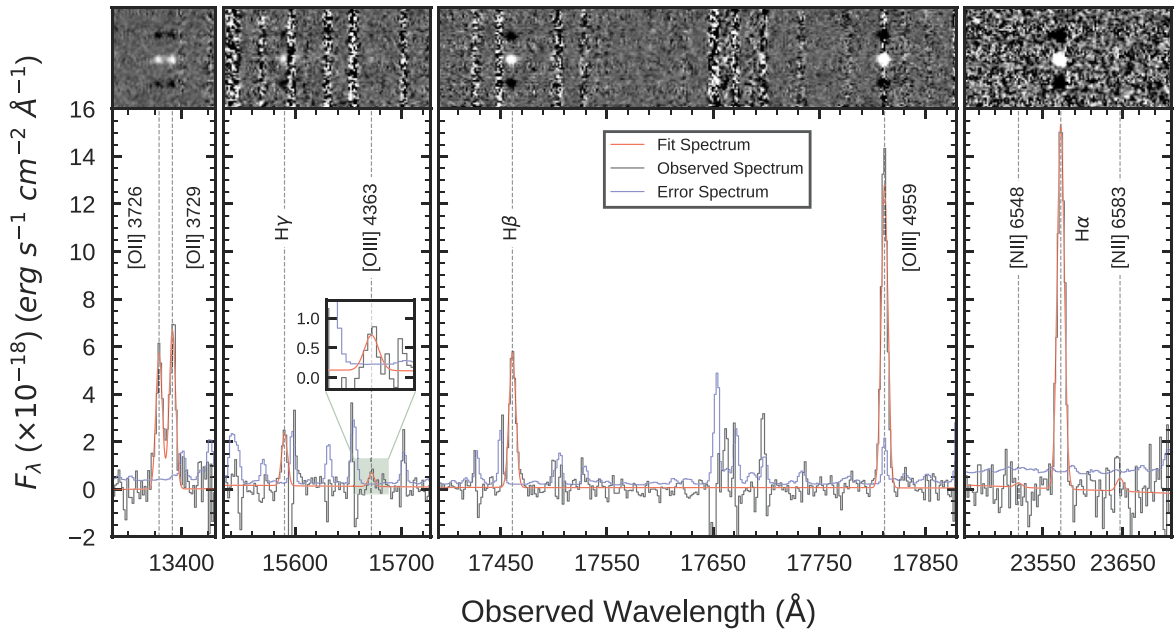


Figure 2. The $z = 2.5918$ observed spectrum of A1689-217 in the J , H , and K bands of Keck/MOSFIRE. The top panel shows the 2D spectrum, while the bottom panel shows the observed (black), error (blue), and single-Gaussian fit (red) spectra in one dimension. The emission lines are labeled for reference. The portion of the spectrum containing [O III] $\lambda 4363$ has been highlighted in green and magnified in the inset plot. A peak can be seen at the observed location of the line among 4 consecutive pixels with $S/N > 1$. We report a total significance in the detection of 4.2σ . Emission of [O III] $\lambda 4363$ in the 2D spectrum is also visible, along with the expected symmetric negative images on either side resulting from nodding along the slit.

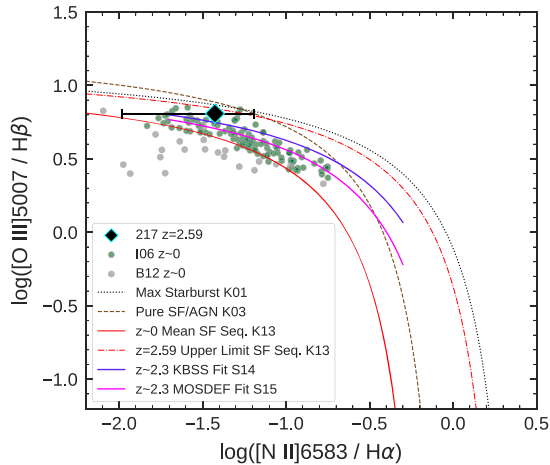


Figure 3. [O III] $\lambda 5007/H\beta$ vs. [N II] $\lambda 6583/H\alpha$ N2-BPT diagram. A1689-217 is denoted by the black diamond with cyan border and lies offset from the $z \sim 0$ mean star-forming sequence of Kewley et al. (2013, K13) (solid red line). The galaxy displays high excitation and a very low [N II]/ $H\alpha$ ratio, with the large error bars resulting from the lack of a significant [N II] $\lambda 6583$ detection. The green and gray points represent the $z \sim 0$ comparison samples (see Section 5) of Izotov et al. (2006, I06) and Berg et al. (2012, B12), respectively. The dotted black line is the “maximum starburst” curve from Kewley et al. (2001, K01). The dashed brown line is the demarcation between star-forming galaxies and AGNs from Kauffmann et al. (2003, K03). The purple line is the best fit to the $z \sim 2.3$ star-forming galaxies in Steidel et al. (2014, S14), while the magenta line is the best fit to the $z \sim 2.3$ star-forming galaxies in Shapley et al. (2015, S15). The red dotted-dashed line represents the theoretical $z = 2.59$ upper-limit, star-forming abundance sequence as given by Kewley et al. (2013, K13).

3.2. Fitting the Spectrum

The spectrum of A1689-217 was fit using the Markov Chain Monte Carlo Ensemble sampler `emcee`⁷ (Foreman-Mackey

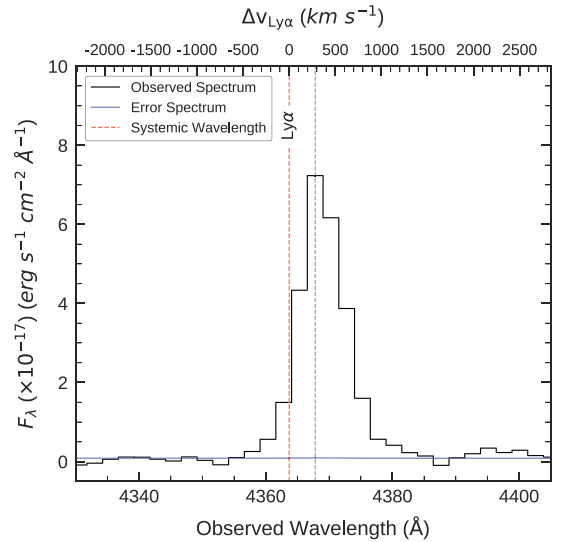


Figure 4. Ly α emission line of A1689-217, observed with Keck/LRIS. The observed and error spectra are shown in black and blue, respectively. The systemic wavelength of Ly α is denoted by the dashed red line. The observed peak of the Ly α line, marked by the dashed gray line, displays a velocity offset (labeled on the upper x-axis) from the systemic redshift of $\Delta v_{Ly\alpha} = 282 \text{ km s}^{-1}$.

et al. 2013). In each filter we fit single-Gaussian profiles to the emission lines and a line to the continuum. In the H band, due to the large wavelength separation between $H\beta$ and [O III] $\lambda 4363$, $H\beta$ and [O III] $\lambda 4959$ were fit separately from $H\gamma$ and [O III] $\lambda 4363$. While the width and redshift were free parameters in the H and K bands, in the H band they were only fit with the much higher S/N lines of $H\beta$ and [O III] $\lambda 4959$ and then adopted for $H\gamma$ and [O III] $\lambda 4363$. In the J band, due to the small wavelength separation of

⁷ <https://emcee.readthedocs.io/en/v2.2.1/>

Table 1
Emission-line Fluxes and EWs for A1689-217

Line	λ_{rest}^a	λ_{obs}	f_{obs}^b	$f_{\text{corr}}^{b,c}$
[O II]	3726.03	13 383.21	40.8 ± 1.7	222 ± 9
[O II]	3728.82	13 393.21	47.3 ± 2.2	257 ± 12
$H\gamma^d$	4340.46	15 590.12	18.3 ± 1.4	81 ± 6
[O III]	4363.21	15 671.84	4.8 ± 1.1	21 ± 5
$H\beta^d$	4861.32	17 460.96	53.2 ± 1.4	192 ± 5
[O III]	4958.91	17 811.48	118.7 ± 4.9	414 ± 17
$H\alpha^d$	6562.79	23 572.34	206.0 ± 6.9	507 ± 17
[N II]	6583.45	23 646.52	7.8 ± 5.6	19 ± 14
$EW_0(\text{Ly}\alpha)^e$				$137.9^{+8.3}_{-8.5}$
$EW_0([\text{O III}] \lambda 5007)$				860.4 ± 52.2
$EW_0(H\alpha)$				520.7 ± 28.7

Notes. The [O III] $\lambda 5007$ line lies at the edge of the H -band filter, so the flux for this line is found via the intrinsic flux ratio of the doublet: [O III] $\lambda 5007$ /[O III] $\lambda 4959 = 2.98$.

^a Rest-frame wavelengths in air (\AA).

^b Fluxes are in units of $10^{-18} \text{ erg s}^{-1} \text{ cm}^{-2}$ and are uncorrected for lens magnification. f_{obs} and f_{corr} refer to the observed and dust-corrected fluxes, respectively. Both f_{obs} and f_{corr} are slit loss corrected.

^c The intrinsic flux uncertainties do not include other systematic errors associated with interfilter calibrations and dust correction, though these additional errors are propagated throughout all of our calculations.

^d Emission-line fluxes not corrected for underlying stellar absorption, as these corrections are small and uncertain (see Section 4.2).

^e Rest-frame equivalent widths in \AA .

the [O II] doublet, and thus the partial blending of the lines (seen in Figure 2), the redshift and width were taken to be the values fit to the highest-S/N line in the spectrum ($H\beta$). The redshift of A1689-217 reported in this paper (see Table 2) is the weighted average of the redshifts fit to the H and K bands.

4. Properties of A1689-217

Estimates of various physical properties of A1689-217 are summarized in Table 2, with select properties discussed in greater detail in the sections below.

4.1. Stellar Mass and Age

The stellar mass is estimated by fitting stellar population synthesis models to the HST optical and near-IR photometry. Because some of the emission lines have high equivalent widths (see Table 1), we have corrected the photometry by subtracting the contribution from the emission lines (e.g., $\text{Ly}\alpha$, [O II] $\lambda\lambda 3726, 3729$, $H\gamma$, [O III] $\lambda 4363$). We have also added in quadrature an additional 3% flux error in all bands to account for systematic errors in the photometry (Alavi et al. 2016). We use the stellar population fitting code FAST⁸ (Kriek et al. 2009) with the Bruzual & Charlot (2003) stellar population synthesis models and a constant SFR with a Chabrier initial mass function (IMF; Chabrier 2003). As suggested by Reddy et al. (2018) for high-redshift, low-mass galaxies, we use the SMC dust extinction curve (Gordon et al. 2003), with A_V values varying between 0.0 and 2.0. We fix the metallicity at $0.2 Z_\odot$ and the redshift at the spectroscopic value. The stellar age can vary between $7.0 < \log(t) [\text{yr}] < 10.0$. The

Table 2
Properties of A1689-217

Property	Value
R.A. (J2000)	$13^{\text{h}} 11^{\text{m}} 27^{\text{s}}.62$
Decl. (J2000)	$-01^{\circ} 21' 35''.62$
z	$2.591 81$ $\pm 0.000 01$
μ	7.89 ± 0.40
$\log(M_*/M_\odot)^{a,b}$	$8.07\text{--}8.59$
$M_{\text{UV},1700}^a$	-18.67 ± 0.04
$E(B - V)_{\text{gas}}$	0.39 ± 0.05
$\text{SFR}^a (M_\odot \text{ yr}^{-1})$	16.2 ± 1.8
$n_e (\text{cm}^{-3})$	220^{+70}_{-60}
$T_e([\text{O II}]) (\text{K})$	$13,000 \pm 1100$
$T_e([\text{O III}]) (\text{K})$	$14,300 \pm 1500$
$12 + \log(\text{O}^+/\text{H}^+)$	7.56 ± 0.12
$12 + \log(\text{O}^{++}/\text{H}^+)$	7.90 ± 0.12
$12 + \log(\text{O}/\text{H})$	8.06 ± 0.12
$Z (Z_\odot)$	$0.24^{+0.08}_{-0.06}$

Notes.

^a Most probable value corrected for the listed magnification factor, μ . The uncertainty does not include the uncertainty in the magnification.

^b The lower and upper bounds of the stellar-mass estimate. The lower bound corresponds to our best-fit SED model ($t \sim 50$ Myr), and the upper bound corresponds to a young stellar component ($t = 50$ Myr) in combination with a 1.6 Gyr old burst component. See Section 4.1 and Figure 5 for further details.

1σ confidence intervals are derived from a Monte Carlo method of perturbing the broadband photometry within the corresponding photometric uncertainties and refitting the spectral energy distribution (SED) 300 times. The best-fit parameters for A1689-217, corrected for the lensing magnification factor, $\mu = 7.89$, when necessary, are $A_V = 0.25$, $\log(M_*/M_\odot) = 8.07$, $\text{SFR} = 2.75 M_\odot \text{ yr}^{-1}$, and $t_{\text{age}} \sim 50$ Myr, with the best-fit, demagnified SED model shown in Figure 5.

The young age of the stellar population is perhaps not surprising, as the large $H\alpha$ equivalent width ($EW_{0,H\alpha} = 521 \text{ \AA}$) strongly suggests that A1689-217 is undergoing an intense burst of star formation, as seen in a subset of galaxies at high redshift (Atek et al. 2011, 2014; Straughn et al. 2011; van der Wel et al. 2011; Tang et al. 2019). Because the stellar population associated with this recent burst is young, it has a low mass-to-light ratio and can easily be hiding a significant mass in older stars. To understand how much stellar mass we might be missing, we investigated adding a maximally old stellar population, formed in a single burst at $z = 6$ (1.6 Gyr old at $z = 2.5918$). We found that the stellar mass could be increased by a factor of 3.3 before the reduced χ^2 is increased by a factor of two (seen in Figure 5). Thus, we use $3.3 \times$ the mass from the SED fit, or $\log(M_*/M_\odot) < 8.59$, as the upper limit of the stellar mass.

We note that many of the high-redshift galaxies with [O III] $\lambda 4363$ detections have high equivalent width Balmer lines and may selectively be in a burst relative to the typical galaxy at these redshifts (Ly et al. 2015). Thus, a simple star formation history fit to the photometry might be dominated by the recent burst and will significantly underestimate the stellar mass. This is important to consider when ultimately trying to measure the MZR with these galaxies.

⁸ <http://w.astro.berkeley.edu/~mariska/FAST.html>

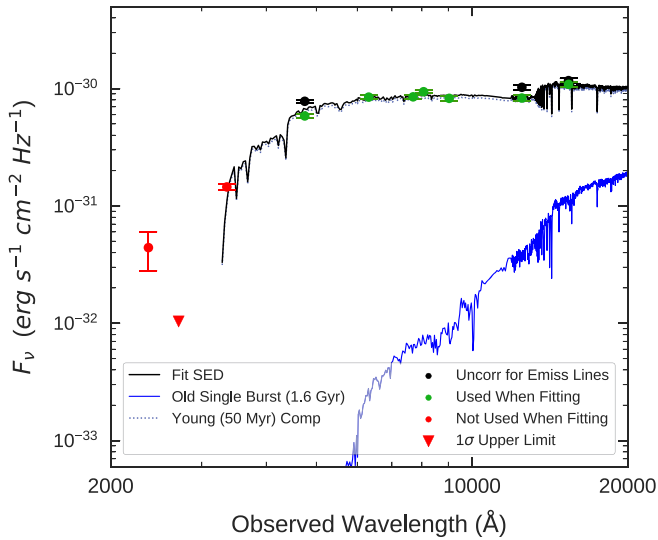


Figure 5. Demagnified, observed photometry and best-fit SED model (black line) for A1689-217. The green data points represent the emission-line-subtracted photometry used for the SED fitting. The black data points represent the photometry before correction for emission lines. The red points signify WFC3/UVIS photometry not used in the fitting because of Ly α forest absorption. An additional 3% flux error, used to account for systematic errors in the photometry, has been added in quadrature to the flux errors in each of the bands prior to SED fitting and is reflected in the error bars of all (green, black, and red) photometric data points. The SED redshift is fixed to the spectroscopic value of $z_{\text{spec}} = 2.5918$. The best-fit model indicates a young stellar population (~ 50 Myr). Also plotted is a maximally old (1.6 Gyr) stellar population (blue solid line) that can be added to the fit while slightly scaling down the best-fit, constant-SFR SED (blue dotted line). Adding this older component can increase the stellar mass by a factor of 3.3 at a doubling of the reduced χ^2 , so it is treated as an upper limit to the stellar mass.

4.2. Nebular Extinction and SFR

To properly estimate galactic properties and conditions within the ISM, several of which rely on flux ratios, the wavelength-dependent extinction from dust must be accounted for. This extinction can be quantified with Balmer line ratios calculated from observed hydrogen emission-line fluxes. With the strong detections of H γ , H β , and H α in the spectrum of A1689-217, we estimate the extinction due to dust by assuming case B intrinsic ratios of H α /H β = 2.79 and H α /H γ = 5.90 for $T_e = 15,000$ K and $n_e = 100$ cm $^{-3}$ (Dopita & Sutherland 2003), approximately the electron temperature and density of A1689-217 (see Section 4.3).⁹ We note the presence of underlying stellar absorption of the Balmer lines in Figure 5 but do not make any corrections to the emission-line fluxes of H γ , H β , or H α here, as these corrections amount to small percentage differences in the fluxes of $\sim 3.5\%$, $\sim 1.1\%$, and $\sim 0.1\%$, respectively, and are also based on an uncertain star formation history. Assuming the extinction curve of Cardelli et al. (1989) with an $R_V = 3.1$, we find the color excess to be $E(B - V)_{\text{gas}} = A_V/R_V = 0.39 \pm 0.05$. We use this result to correct the observed emission-line fluxes for extinction due to dust and list the corrected values in Table 1. We note that the nebular extinction is significantly higher than the best-fit extinction of the stellar continuum derived from the SED fit ($A_V = 0.25$) and indicated by the flat (in f_ν) SED seen in

⁹ The variation in the intrinsic Balmer line ratios with temperature is small over the temperature range typical of H II regions. We obtain $T_e \sim 15,000$ K after correcting for dust regardless of using the Balmer ratios corresponding to 15,000 K or the commonly assumed 10,000 K.

Figure 5. This difference in nebular versus stellar extinction is likely due to the young age of the burst, indicating that the nebular regions are still enshrouded within their birth cloud (Charlot & Fall 2000). We also note here that some T_e -derived metallicities at high redshift are calculated with dust corrections based on the stellar SEDs. If many of these galaxies are in a burst of recent star formation, the stellar attenuation may not be a reliable indicator of the nebular extinction. This is especially concerning for galaxies with O III] $\lambda\lambda 1661, 1666$ detections (rest-UV auroral lines used to estimate T_e) instead of [O III] $\lambda 4363$, as the attenuation at these wavelengths is much larger.

The SFR of A1689-217 is calculated with the galaxy’s dust-corrected H α luminosity ($L(\text{H}\alpha)$) and the relation between SFR and $L(\text{H}\alpha)$ from Kennicutt (1998). The conversion factor of the relation is recalculated assuming a Chabrier (2003) IMF with $0.2 Z_\odot$, roughly the oxygen abundance of A1689-217 (see Section 4.4). The resulting SFR is divided by the magnification factor ($\mu = 7.89$) from the lensing model. We estimate that A1689-217 has an SFR = $16.2 \pm 1.8 M_\odot \text{ yr}^{-1}$. The uncertainty in this measurement does not include the uncertainty in the magnification, as the magnification and its error are dependent on the assumptions inherent to the lensing model. We also note here that the H α -derived SFR is nearly six times larger than the SED-derived SFR. Much of this discrepancy can be explained if the stellar population has a harder ionizing spectrum due to low Fe abundance (Steidel et al. 2014) and/or binary stellar evolution (Eldridge & Stanway 2009). A harder ionizing spectrum produces more ionizing photons, seen in the H α recombination line, relative to the nonionizing UV and thus should yield H α -based SFRs that are larger than those derived via fitting to rest-UV photometry.

4.3. Electron Temperature and Density

The electron temperature (T_e) and electron density (n_e) are intrinsic nebular properties that are responsible for the strength of collisionally excited lines that allow for a direct measurement of the gas-phase metallicity of H II regions. We calculate the electron temperature in the O $^{++}$ region, $T_e(\text{[O III]})$, using the temperature-sensitive line ratio [O III] $\lambda\lambda 4959, 5007$ /[O III] $\lambda 4363$ and the IRAF task NEBULAR.TEMDEN (Shaw & Dufour 1994). This temperature-sensitive ratio is dependent on electron density, though below $n_e \approx 10^3$ cm $^{-3}$ —the low-density regime within which A1689-217 and this paper’s literature comparison sample reside— $T_e(\text{[O III]})$ is insensitive to the density (Osterbrock & Ferland 2006). We therefore calculate $T_e(\text{[O III]})$ noniteratively, assuming a fiducial electron density of $n_e = 150$ cm $^{-3}$, appropriate for H II regions (Sanders et al. 2016a). This yields a result of $T_e(\text{[O III]}) = 14,300 \pm 1500$ K.¹⁰ To calculate the electron temperature in the O $^+$ region, $T_e(\text{[O II]})$, the auroral doublet [O II] $\lambda\lambda 7320, 7330$ is needed. These lines are not within our wavelength coverage, so we utilize the $T_e(\text{[O III]})$ – $T_e(\text{[O II]})$ relation of Campbell et al. (1986) to obtain an electron temperature in the O $^+$ region of $T_e(\text{[O II]}) = 13,000 \pm 1100$ K.

The electron density is estimated with the doublet ratio [O II] $\lambda 3729$ /[O II] $\lambda 3726$ and the IRAF task NEBULAR.TEMDEN. The aforementioned $T_e(\text{[O II]}) = 13,000$ K is used in the calculation. We obtain an electron density for A1689-217 of $n_e = 220_{-60}^{+70}$ cm $^{-3}$. This measurement is consistent with the

¹⁰ Assuming any $n_e < 1000$ cm $^{-3}$ results in variations of our calculated T_e of $< 0.5\%$.

typical electron density found by Sanders et al. (2016a) for $z \sim 2.3$ star-forming galaxies, $\sim 250 \text{ cm}^{-3}$, a factor of ~ 10 higher than densities in local star-forming regions. It should be noted, however, that while our measurement agrees with Sanders et al. (2016a) and others (e.g., Steidel et al. 2014; Kashino et al. 2017), our galaxy is $\sim 0.9\text{--}1.4$ dex lower in stellar mass (see Section 4.1 and Figure 5) than the mass ($\sim 10^{9.5} M_{\odot}$) above which Sanders et al. (2016a) are confident that their density estimate holds true.

4.4. Oxygen Abundance

The oxygen abundance, or gas-phase metallicity, is calculated using the analytic ionic abundance expressions of Izotov et al. (2006). These equations make use of the values found for $T_e(\text{[O II]})$, $T_e(\text{[O III]})$, and n_e from the previous section. We assume that the oxygen abundance comprises contributions from the populations of the O^+ and O^{++} zones of an H II region with negligible contributions from higher oxygen ionization states

$$\frac{\text{O}}{\text{H}} \approx \frac{\text{O}^+}{\text{H}^+} + \frac{\text{O}^{++}}{\text{H}^+}. \quad (1)$$

We calculate an oxygen abundance for A1689-217 of $12 + \log(\text{O}/\text{H}) = 8.06 \pm 0.12$ ($0.24 Z_{\odot}$; Asplund et al. 2009).

4.5. Uncertainties

To calculate the 1σ uncertainties of the intrinsic emission-line fluxes, flux ratios, and other properties of A1689-217, we utilize a Monte Carlo approach in which a given value is sampled $N = 10^5$ times. The uncertainties in the intrinsic emission-line fluxes are found by first sampling the probability distribution of A1689-217’s extinction in the visual band (A_V), needed for the extinction at a given wavelength (A_{λ}), and the probability distribution of each emission line’s observed flux. The final probability distribution of A_V is the result of multiplying the probability distributions of A_V found for each of the Balmer decrements considered for A1689-217, $\text{H}\alpha/\text{H}\beta$ and $\text{H}\alpha/\text{H}\gamma$, with the uncertainty for each ratio coming from its observed statistical error added in quadrature with a 5% interfilter systematic error. The visual-band extinction and the emission lines are each sampled N times from a normal distribution centered on the most probable A_V or observed flux, respectively, with a standard deviation given by the 1σ error of the value being sampled. The A_V values are then used to calculate N extinction magnitudes for each emission line, with which each iteration of each emission-line sample is dust corrected, giving a sample of N intrinsic fluxes for each line. A posterior histogram is then generated for the intrinsic flux of each line, and a 68% confidence interval is fit, allowing a 1σ uncertainty to be determined for each line’s intrinsic flux.

In the calculation of the flux ratio uncertainties, we take the samples of intrinsic emission-line fluxes and calculate N -length samples of the desired flux ratios, for which posterior histograms are created and 1σ errors estimated as for the intrinsic emission-line fluxes. The properties of A1689-217 have their uncertainties estimated in the same manner.

5. Discussion

5.1. Strong-line Ratio–Metallicity Diagnostics

Having calculated the intrinsic emission-line fluxes and direct-metallicity estimate of A1689-217, we study the evolution of both nebular physical properties and the relationships between strong-line ratios and T_e -based metallicities.

Jones et al. (2015) presented the first calibrations between strong-line ratios and direct metallicities at significant redshift, utilizing a sample of 32 star-forming galaxies at $z \sim 0.8$ from the DEEP2 Galaxy Redshift Survey (Davis et al. 2003; Newman et al. 2013). Because the flux ratio of $[\text{O III}] \lambda 4363 / [\text{O III}] \lambda 5007$ is generally $\lesssim 3\%$, random noise creates a large scatter in the measurement of this temperature-sensitive ratio. To combat this effect, all 32 galaxies in the Jones et al. sample were selected because they have high S/N in $[\text{O III}] \lambda 5007$ and low noise in the location of $[\text{O III}] \lambda 4363$. More specifically, the galaxies in the sample have a ratio of $[\text{O III}] \lambda 5007$ flux to uncertainty in the $[\text{O III}] \lambda 4363$ flux (f_{5007}/σ_{4363}) of ≥ 300 . This ratio, which they call the “sensitivity” (this term used hereafter to denote this ratio), reduces not only the effects of random noise but also the bias toward very low metallicity ($12 + \log(\text{O}/\text{H}) \lesssim 8.3\text{--}8.4$ or $Z \lesssim 0.4\text{--}0.5 Z_{\odot}$) galaxies that comes with selecting a sample via $[\text{O III}] \lambda 4363$ significance instead (see their Figure 1).

Jones et al. (2015) found that the relations between direct metallicity and ratios of neon, oxygen, and hydrogen emission lines derived from their sample are consistent (albeit with larger uncertainties) with the relations derived from a subset (subject to the same sensitivity requirement) of the $z \sim 0$ star-forming galaxies from Izotov et al. (2006)—a subsample itself from Data Release 3 of the SDSS (Abazajian et al. 2005). Jones et al. showed that these relations do not evolve from $z = 0$ to $z \sim 0.8$.

5.1.1. Comparison Samples across Cosmic Time

In a similar manner to Jones et al. (2015) and Sanders et al. (2016b) with their object COSMOS-1908, we will use the measurements of A1689-217, compared to other $[\text{O III}] \lambda 4363$ sources at various redshifts, to further study the evolution of the calibrations in Jones et al. (2015), particularly at higher redshift. We note that unlike in Jones et al. (2015) and Sanders et al. (2016b), the relations involving $[\text{Ne III}] \lambda 3869$ are not studied here because this line falls out of our spectroscopic coverage of A1689-217.

In addition to the 32 $z \sim 0.8$ galaxies from Jones et al. (2015), we also consider two local $z \sim 0$ comparison samples: 113 star-forming galaxies with spectral coverage of the optical $[\text{O II}]$ doublet from Izotov et al. (2006)—the same $z \sim 0$ sample used in Jones et al. (2015)—and 28 H II regions (21 total galaxies) from Berg et al. (2012). The galaxies from Berg et al. (2012) compose a low-luminosity subsample of the *Spitzer* Local Volume Legacy (LVL) catalog (Dale et al. 2009) and have high-resolution MMT spectroscopy for $[\text{O III}] \lambda 4363$ detection. This particular sample was chosen because of its low luminosity and the volume-limited—as opposed to flux-limited—nature of its parent LVL sample, the combination of which allows for the statistical study of local dwarf galaxies ($5.90 \leq \log(M_*/M_{\odot}) \leq 9.43$ here). These Berg et al. sample qualities are similar to those of our high- z parent survey, to which A1689-217 belongs, in the sense that we are looking at

very low mass objects (via lensing) in a small volume as opposed to less typical, more luminous objects in a larger volume.

Both of the local comparison samples adhere to the sensitivity cut placed on the Jones et al. (2015) sample. Additionally, as in Izotov et al. (2006), we arrived at our stated comparison sample sizes by removing all galaxies (or H II regions) with both $[\text{O III}] \lambda 4959/\text{H}\beta < 0.7$ and $[\text{O II}] \lambda 3727/\text{H}\beta > 1.0$, ensuring high-excitation samples that do not discriminate against very metal-deficient sources with high excitation. Global oxygen abundance and strong-line ratio values for galaxies in the Berg et al. (2012) sample with multiple H II regions meeting these cuts are taken as the average of the individual H II region values, weighted by the uncertainties calculated for the abundances and ratios, respectively, as detailed in Section 4.5.

At low to intermediate redshifts, we also include 9 of the 20 $z < 0.9$, high specific SFR (sSFR) galaxies with $[\text{O III}] \lambda 4363$ detections from Ly et al. (2014) and the Subaru Deep Field (Kashikawa et al. 2004), excluding the rest of the sample owing to the inability to determine dust corrections, unreliable T_e estimates, missing $\text{H}\beta$ or stellar mass (necessary for our study of the FMR in Section 5.4), and the presence of a LINER. Due to this sample being so small, we do not apply the sensitivity cut of Jones et al. (2015), which would remove five of the nine objects, but note that all galaxies pass the cut of Izotov et al. (2006).

In addition to the low- and intermediate-redshift samples, we also compare A1689-217 to the galaxies of James et al. (2014) at $z = 1.43$, Stark et al. (2013) at $z = 1.43$, Christensen et al. (2012) at $z = 1.83$, and Sanders et al. (2016b) at $z = 3.08$. Each of these galaxies has an $[\text{O III}] \lambda 4363$ detection and a corresponding, recalculated, direct-metallicity estimate. We do not compare to the galaxy reported in Yuan & Kewley (2009), as our deeper spectrum of this galaxy shows that the claimed $[\text{O III}] \lambda 4363$ detection is not correct. See the Appendix for more details. All comparison samples in this paper, at $z \sim 0\text{--}3.1$, are dust corrected using the Cardelli et al. (1989) extinction curve, with an $R_V = 3.1$ (except for Jones et al. 2015, who use an $R_V = 4.05$ but show that their results are insensitive to this value), and have had their physical properties recalculated using the methods detailed in Sections 4.3 and 4.4.

We do not include any $[\text{O III}] \lambda 1661, 1666$ sources in our comparison samples as do some other similar studies (e.g., Patrício et al. 2018; Sanders et al. 2019) owing to added complications when considering both the optical and ultraviolet. These complications lie primarily in the very uncertain extinction law in the UV and the large wavelength separation between these auroral lines and $[\text{O III}] \lambda 5007$, as well as in issues arising from observing in these different regimes (e.g., different instruments, slit widths, seeing).

5.1.2. The Evolution of the Strong-line Ratio–Metallicity Calibrations

In our effort to further quantify the evolution at high redshift of the locally calibrated, strong-line metallicity relations, as well as other physical properties, we consider the positions of A1689-217 and the other high-redshift galaxies in relation to the Jones et al. (2015) calibrations and other lower-redshift comparison samples in the four panels of Figure 6. We find that A1689-217 is consistent with the local best-fit relations of Jones et al. (2015) in the top two and bottom left panels, given A1689-217’s uncertainties and the relations’ intrinsic scatter.

We observe A1689-217 to be $\sim 1.6\sigma$ above the best-fit R_{23} (see Equation (3) for R_{23} ratio) relation at its metallicity of $Z = 8.06$, though we do not claim it to be inconsistent with the relation based on A1689-217’s uncertainties in both parameters, especially oxygen abundance, combined with the scatter around the relation. A1689-217’s elevated R_{23} value is a consequence of A1689-217 being above the local relation in the $[\text{O III}] \lambda 5007/\text{H}\beta$ ratio and especially in the $[\text{O II}] \lambda 3726, 3729/\text{H}\beta$ ratio, though both ratios are consistent with the local calibrations. When also considering the other $z > 1$ sources in addition to A1689-217, we do not observe any significant systematic offsets in line ratio or metallicity for any of the relations. We therefore suggest that there is no evidence of evolution from $z \sim 0$ to $z \sim 3.1$ in the relations between direct metallicity and emission-line ratios involving only oxygen and hydrogen. However, larger samples of $[\text{O III}] \lambda 4363$ detections are needed in order to significantly constrain the evolution out to high redshift.

We do caution, however, that four out of the five $z > 1$ galaxies lie at or very near the turnover portion of the $[\text{O III}] \lambda 5007/\text{H}\beta$ and R_{23} relations, where variation in the strong-line ratio is small over the corresponding oxygen abundance range, limiting the constraining power of the relations when determining the metallicity at fixed line ratio. This is seen as well in the recent work of Sanders et al. (2019), who study the relationships between strong-line ratios and direct metallicity using a sample of 18 galaxies at $1.4 \lesssim z \lesssim 3.6$ with $[\text{O III}] \lambda 4363$ or $[\text{O III}] \lambda 1661, 1666$ auroral-line detections, including three new $[\text{O III}] \lambda 4363$ detections from the MOSFIRE Deep Evolution Field survey (MOSDEF; Kriek et al. 2015). They show an abundance of objects with $7.7 < 12 + \log(\text{O}/\text{H}) < 8.1$ lying at these turnovers and caution against the use of these line ratios at high z for galaxies within this metallicity regime.

In addition to the strong-line metallicity relations of Jones et al. (2015), we plot the $[\text{O III}]/[\text{O II}]$ —direct-metallicity calibration of Bian et al. (2018) (top left panel of Figure 6), who utilized stacked spectra with $[\text{O III}] \lambda 4363$ of $z \sim 0$ high- z analogs that lie at the same location on the N2-BPT diagram as $z \sim 2.3$ star-forming galaxies. This calibration is favored in Sanders et al. (2019) for its linear relation between the strong-line ratio and metallicity, its ability to closely reproduce (~ 0.1 dex) the average metallicity of their $z > 1$ sample, and its derivation from an analog sample selected via strong-line ratios rather than global galaxy properties. Within the range of applicability, $12 + \log(\text{O}/\text{H}) = 7.8\text{--}8.4$, there is generally good agreement between the relation, our various samples (including A1689-217), and the relation of Jones et al. (2015), as the relation of Bian et al. (2018) lies within the intrinsic scatter around that of Jones et al. (2015).

We note that the majority of the Berg et al. (2012) line ratios do not follow the local relations with direct metallicity. While there is good agreement between the local Jones et al. relations and the few H II regions in the Berg et al. sample with $8.2 \lesssim 12 + \log(\text{O}/\text{H}) \lesssim 8.4$, the bulk of the H II region sample, having $12 + \log(\text{O}/\text{H}) \lesssim 8.1$, lies removed from these relations. This is seen as well in the strong-line ratio—direct-metallicity plots of Sanders et al. (2019, Figure 3), who find agreement at $12 + \log(\text{O}/\text{H}) \sim 8.3$ between the median relations of individual $z = 0$ H II regions and their $z \sim 0$ and $z > 1$ galaxy samples, but similar divergences below an oxygen abundance of ~ 8.0 . As Sanders et al. suggest, this

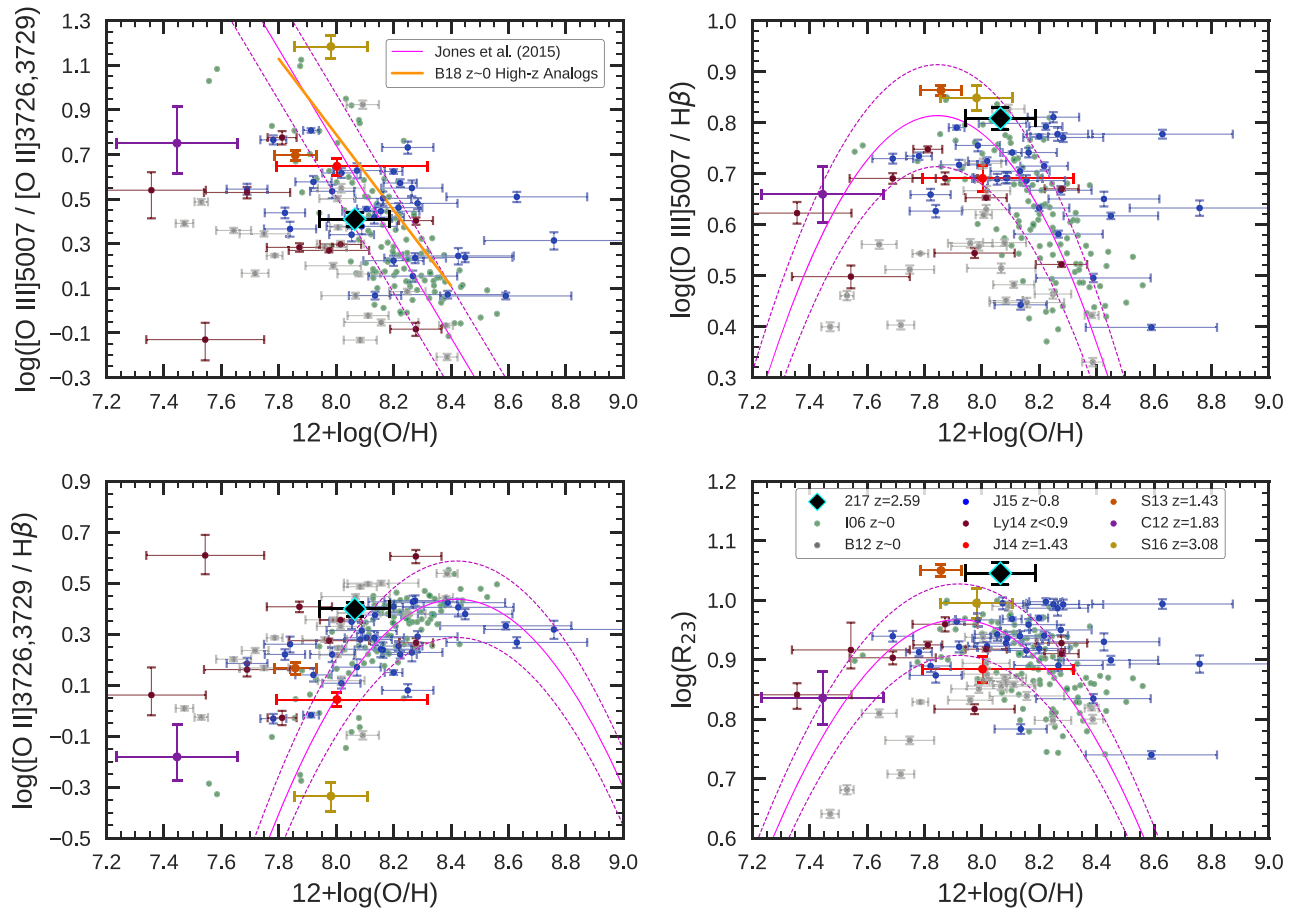


Figure 6. Strong emission-line ratios vs. direct-method oxygen abundance for A1689-217 and comparison samples ranging in redshift from $z \sim 0$ to $z \sim 3.1$. A1689-217 is denoted by the black diamond with cyan border. The $z \sim 0.8$ sample of Jones et al. (2015, J15) is given by the blue data points. The $z < 0.9$ sample of Ly et al. (2014, Ly14) is given by the dark-red data points. The red, dark-orange, purple, and gold points correspond to the $z = 1.43$ galaxy of James et al. (2014, J14), the $z = 1.43$ galaxy of Stark et al. (2013, S13), the $z = 1.83$ galaxy of Christensen et al. (2012, C12), and the $z = 3.08$ galaxy of Sanders et al. (2016b, S16), respectively. The solid magenta lines show the best-fit relations between the strong-line ratios and metallicity as determined by Jones et al. (2015) with the $z \sim 0$ Izotov et al. (2006) sample. The accompanying dashed magenta lines represent the 1σ intrinsic scatter around the best-fit relations. The orange line in the top left panel is the best-fit relation, based on stacked spectra of $z \sim 0$ high- z analogs, of Bian et al. (2018, B18). The sample of Berg et al. (2012, B12) $z \sim 0$ LVL galaxies is represented by the gray points and included to show the disparity between this low-excitation (see also Figure 3), low- $sSFR$ (median $sSFR \sim 0.2 \text{ Gyr}^{-1}$ for the objects used here) sample and the other comparison samples when investigating these strong-line ratio-metallicity relations.

may be due to an incomplete sample of local, high-excitation, low-metallicity H II regions, possibly a result of the short-lived nature of individual star-forming regions and their rapidly changing ionizing spectra.

5.2. O_{32} versus R_{23} Excitation Diagram and Its Use as a Metallicity Indicator

The O_{32} versus R_{23} excitation diagram relates optical emission-line ratios given by the following equations:

$$O_{32} = \frac{[\text{O III}]\lambda\lambda 4959, 5007}{[\text{O II}]\lambda\lambda 3726, 3729} \quad (2)$$

$$R_{23} = \frac{[\text{O II}]\lambda\lambda 3726, 3729 + [\text{O III}]\lambda\lambda 4959, 5007}{H\beta} \quad (3)$$

As seen in the high-excitation tail of O_{32} versus R_{23} displayed in Figure 7 for A1689-217 and the comparison samples, as well as in full in the literature (e.g., Nakajima et al. 2013; Nakajima & Ouchi 2014; Shapley et al. 2015; Sanders et al. 2016a; Strom et al. 2017), the excitation diagram characteristically has a strong correlation between higher O_{32} and R_{23} values. It has

also been shown by Nakajima & Ouchi (2014) with a sample of $z = 2-3$ Lyman break galaxies, by Shapley et al. (2015) and Sanders et al. (2016a) with $z \sim 2.3$ galaxies from the MOSDEF survey, and by Strom et al. (2017) with $z \sim 2.3$ galaxies from the KBSS survey that high-redshift, star-forming galaxies follow the same distribution as local SDSS galaxies toward higher O_{32} and R_{23} values. Indeed, when looking at the galaxies in the left panel of Figure 7, we see no evidence for significant evolution at any of the redshifts considered by our samples.

Individually, the O_{32} ratio serves as a commonly used diagnostic of the ionization parameter of a star-forming region (see Kewley & Dopita 2002; Sanders et al. 2016a), while the R_{23} ratio is a commonly used diagnostic for the gas-phase oxygen abundance of a star-forming region (Pagel et al. 1979). However, as detailed in Kewley & Dopita (2002), O_{32} is dependent on metallicity, and R_{23} is dependent on the ionization parameter. Furthermore, as seen in Figure 6, the R_{23} diagnostic is double-valued (Kewley & Dopita 2002) and not very sensitive to the majority of the subsolar oxygen abundances studied in this work. The variation of ~ 0.3 dex in

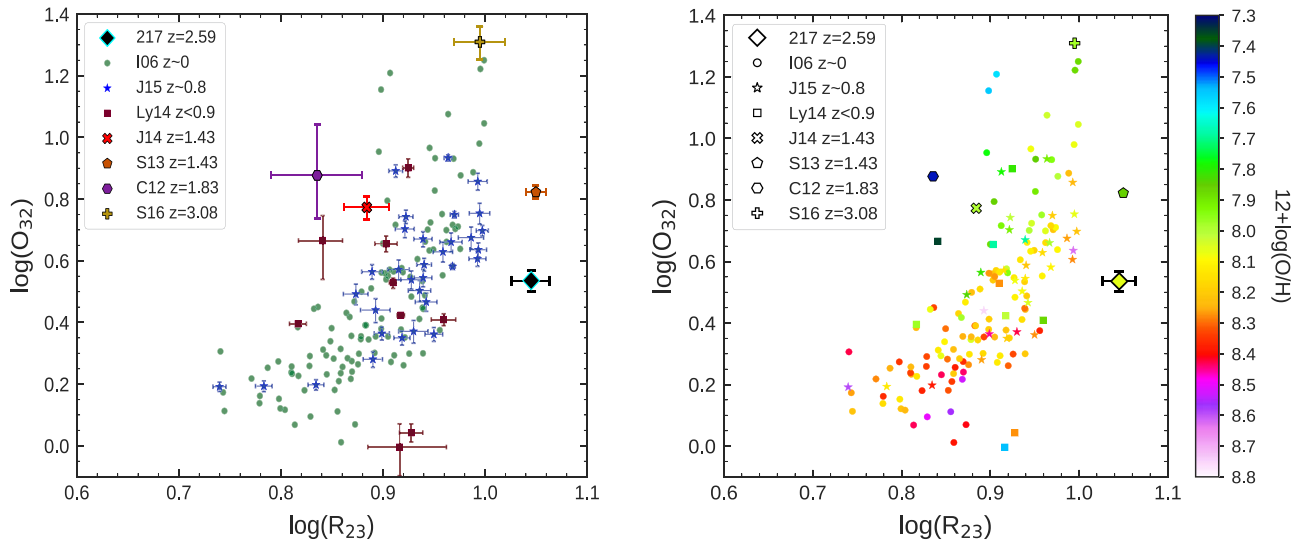


Figure 7. High-excitation tail of the O_{32} vs. R_{23} excitation diagram. Left: A1689-217 and the comparison samples, with error bars, following the same color scheme as in Figure 6. A1689-217 is represented by a diamond with a cyan border. Right: A1689-217 and the comparison samples color-coded by their direct-metallicity estimates. A1689-217 is again represented by a diamond, now with a black border. In both panels, the Izotov et al. (2006, I06) sample is represented by circles. The Jones et al. (2015, J15) sample is represented by stars. The Ly et al. (2014, Ly14) sample is denoted by squares. The James et al. (2014, J14) galaxy, Stark et al. (2013, S13) galaxy, Christensen et al. (2012, C12) galaxy, and Sanders et al. (2016b, S16) galaxy are given by a cross, pentagon, hexagon, and plus sign, respectively. The color mapping of this plot demonstrates the roughly monotonic and redshift-independent decrease in oxygen abundance from low to high O_{32} and R_{23} as first demonstrated empirically by Shapley et al. (2015).

$\log(R_{23})$ seen here in Figures 6 and 7 supports the findings of Steidel et al. (2014, see their Figure 11), who show, via photoionization models, that $\log(R_{23})$ is nearly independent of input oxygen abundance in high-redshift galaxies with gas-phase metallicities ranging from 0.2 to 1.0 Z_{\odot} .

If instead these two ratios are considered simultaneously in the O_{32} versus R_{23} excitation diagram, the double-valued nature of the R_{23} diagnostic is removed, and a combination of ionization parameter and metallicity can be obtained. Kewley & Dopita (2002), Nakajima et al. (2013), Nakajima & Ouchi (2014), and Strom et al. (2018) have all utilized this excitation diagram in combination with photoionization models to calculate oxygen abundances, out to $z \sim 2$ in the latter three studies. Shapley et al. (2015) took an empirical approach to suggesting this excitation diagram’s value as an abundance indicator, using the direct-metallicity estimates from stacked SDSS spectra of Andrews & Martini (2013) to show a nearly monotonic decrease in metallicity from low to high O_{32} and R_{23} . They showed that while R_{23} considered alone does not vary greatly with metallicity, the position within the 2D space defined by these two line ratios correlates strongly with metallicity. They further argued that due to the apparent lack of evolution in high-redshift galaxies along the high-excitation end of the diagram, a redshift-independent (out to $z \sim 2.3$, at least) metallicity calibration deriving from direct abundance estimates could be devised based on the location of a galaxy along the O_{32} versus R_{23} sequence.

We investigate this claim further with A1689-217 and the comparison samples in the right panel of Figure 7. Here we have again plotted A1689-217 and the other samples on the high-excitation tail of the O_{32} versus R_{23} diagram, with each galaxy now color-coded by its direct-metallicity estimate. Unlike in the left panel of Figure 7, we do not plot the error bars for the galaxies (except for A1689-217) so as to more clearly illustrate any present trends. We see that there is indeed a nearly monotonic decrease in metallicity as one moves from the lower $\log(O_{32}) \sim 0.1$ and $\log(R_{23}) \sim 0.8$ along the

sequence to higher values in both ratios. We also note that with redshift there does not appear to be any significant evolution of the samples in either O_{32} or R_{23} , as well as in metallicity. The $z \sim 0$ sample from Izotov et al. (2006) and the $z \sim 0.8$ sample from Jones et al. (2015) track the excitation sequence very similarly, with comparable metallicity values as a function of position along the sequence. The intermediate- and high-redshift galaxies also do not collectively display any systematic offsets in their line ratio values and do not show any evidence of evolution in their metallicities as a function of location on the sequence. These galaxies follow the same metallicity distribution seen by the lower-redshift samples.

We do take note of the large scatter, particularly in $\log(R_{23})$, of the $z > 1$ galaxy sample. At fixed $\log(O_{32})$, the galaxies of Christensen et al. (2012) and James et al. (2014), lie farthest to the left in $\log(R_{23})$ compared to the lower-redshift samples, while the galaxy of Stark et al. (2013) and A1689-217 lie farthest to the right, having significantly higher R_{23} than the comparison samples. This observed scatter may be the consequence of underestimated uncertainties that do not account for systematic errors in the measurement and dust correction of the emission lines, or it may hint at a larger intrinsic scatter in this line ratio at high redshift when compared to the relatively narrow high-excitation tail defined locally. In either case, our conclusions should not be significantly affected, as R_{23} , taken by itself, is not very sensitive to metallicity in the moderately subsolar regime we are studying. A proper analysis of this scatter will require larger statistical samples with well-constrained R_{23} and accurate metallicities that span a broad dynamic range.

The conclusions made from Figure 7 support the findings of Shapley et al. (2015) of the O_{32} versus R_{23} excitation diagram being a useful, redshift-invariant oxygen abundance indicator, based on the direct-metallicity abundance scale, out to at least $z \sim 2.3$ and perhaps $z \sim 3.1$ with the inclusion here of COSMOS-1908 (Sanders et al. 2016b). While much larger samples of intermediate- and high-redshift galaxies with direct-

metallicity estimates are required to confirm or refute the observed lack of evolution in this excitation diagram, its potential as an abundance indicator is important for several reasons (see Jones et al. 2015; Shapley et al. 2015; Sanders et al. 2016a). If this excitation sequence and its relation to metallicity are redshift independent, then a local relation based on the much richer SDSS sample can be developed and applied accurately at high redshift. This sequence and a corresponding abundance calibration are based on line ratios solely involving strong oxygen and hydrogen emission lines, avoiding biases in nitrogen-based abundance indicators resulting from systematically higher N/O abundance ratios at high redshift (Masters et al. 2014; Shapley et al. 2015; Sanders et al. 2016a). Finally, an indicator using this excitation sequence would be based on the direct-metallicity abundance scale, with direct metallicities most closely reflecting the physical conditions present in star-forming regions owing to their relation to electron temperature and density.

5.3. The Evolution of the Ionization Parameter

The ionization parameter, defined as the ratio of the number density of hydrogen-ionizing photons to the number density of hydrogen atoms in the gas, characterizes the ionization state of the gas in a star-forming region and is often determined via the O_{32} (see Equation (2)) line ratio. It has been suggested that at high redshift galaxies have systematically higher ionization parameters than are usually found in local galaxies (Brinchmann et al. 2008; Nakajima et al. 2013; Nakajima & Ouchi 2014; Steidel et al. 2014; Kewley et al. 2015; Cullen et al. 2016; Kashino et al. 2017). These studies have shown this largely based on comparisons at fixed stellar mass (e.g., Kewley et al. 2015; Sanders et al. 2016a), comparison to the average ionization parameter of the entire SDSS (e.g., Nakajima & Ouchi 2014), and comparisons at fixed metallicity (e.g., Cullen et al. 2016; Kashino et al. 2017).

However, studying the $[O\text{ III}] \lambda 5007/[O\text{ II}] \lambda \lambda 3726, 3729$ and $[O\text{ III}] \lambda 5007/H\beta$ ratios at fixed metallicity in Figure 6, we do not see any systematic offset of the high-redshift galaxies toward higher ionization parameter proxy (the former ratio) or higher excitation (the latter ratio) at fixed O/H. This is in agreement with Sanders et al. (2016b), who studied the same high- z comparison galaxies, as well as Sanders et al. (2019), who enlarged their high- z sample with three new $[O\text{ III}] \lambda 4363$ detections from the MOSDEF survey and $O\text{ III}] \lambda \lambda 1661, 1666$ sources from the literature. In regard to the former ratio, A1689-217 ($z = 2.59$) and the $z = 1.43$ galaxy of James et al. (2014) lie very close to the locally calibrated, best-fit relation, within the 1σ intrinsic scatter around the relation. The $z = 3.08$ galaxy of Sanders et al. (2016b) lies above the best-fit relation and scatter, but the $z = 1.43$ galaxy of Stark et al. (2013) and the $z = 1.83$ galaxy of Christensen et al. (2012) lie below them. When considering the latter ratio, all four high-redshift galaxies lie near the best-fit relation within the intrinsic scatter. These results from Figure 6 are corroborated in the O_{32} versus R_{23} excitation diagram of Figure 7. We see no collective systematic offset of these galaxies in O_{32} at fixed R_{23} (a diagnostic for oxygen abundance).

The conclusions drawn from Figures 6 and 7 contrast with studies such as Cullen et al. (2016) and Kashino et al. (2017), who argue for increased ionization parameter at fixed O/H in high-redshift galaxies. Instead, our results support the suggestions of Sanders et al. (2016a, 2016b, 2019), who argue for an

absence of evolution in the ionization parameter at fixed metallicity. Sanders et al. (2016a) used ~ 100 star-forming galaxies at $z \sim 2.3$ from the MOSDEF survey to suggest that while high-redshift galaxies do in fact have systematically higher O_{32} values at fixed stellar mass relative to local galaxies, they have similar O_{32} values at fixed R_{23} . They argue that, with the high-redshift MOSDEF sample following the same distribution as local galaxies along the higher O_{32} and R_{23} end of the excitation sequence, and this end corresponding to lower metallicities (Shapley et al. 2015), the ionization state of high-redshift, star-forming galaxies must be similar to metal-poor local galaxies. This is corroborated by Sanders et al. (2019), who show that, on average, their $z > 1$ auroral-line-emitting sample lies on local relations between ionization parameter and direct-method oxygen abundance, positioned in the same location as metal-poor, $z \sim 0$ SDSS stacks and local H II regions. Sanders et al. (2016a) further argue that the difference in offset when comparing to constant stellar mass as opposed to constant metallicity is due to the evolution of the mass–metallicity relation, where high-redshift galaxies have systematically lower metallicities than local galaxies at fixed stellar mass (Sanders et al. 2015).

It is important to note that the results of this paper support the notion of a lack of evolution in ionization parameter at fixed metallicity without the use of nitrogen in the metallicity estimates. As stated earlier, using direct metallicities and diagnostics (R_{23}) not involving nitrogen avoids possible systematic offsets in the abundance estimates due to higher N/O abundance ratios at high redshift.

5.4. Low-mass End of the FMR

The FMR (Mannucci et al. 2010) is a 3D surface defined by a tight dependence of gas-phase metallicity on stellar mass and SFR and is suggested to exist from $z = 0$ out to $z = 2.5$ without evolution (e.g., Mannucci et al. 2010; Henry et al. 2013; Maiolino & Mannucci 2019). From this surface, Mannucci et al. (2010) define a projection, μ_α versus $12 + \log(O/H)$, where μ_α is a linear combination of stellar mass and SFR relying on the observed correlation and anticorrelation of metallicity with stellar mass and SFR, respectively,

$$\mu_\alpha = \log(M_*) - \alpha \log(\text{SFR}). \quad (4)$$

Mannucci et al. (2010) suggest that if $\alpha = 0.32$ in this relation, the scatter in metallicity at fixed μ_α is minimized, all galaxies out to $z = 2.5$ show the same dependence of metallicity on $\mu_{0.32}$, and all galaxies out to this redshift occupy the same range of $\mu_{0.32}$ values.

Unfortunately, the FMR of Mannucci et al. (2010) is defined by low-redshift SDSS galaxies with stellar masses down to $\log(M_*/M_\odot) = 9.2$, ~ 1.1 (0.6) dex above the lower-limit (upper-limit) stellar mass of A1689-217 (see Section 4.1 and Figure 5). In SFR, this FMR only probes galaxies with $-1.45 \leq \log(\text{SFR}) \leq 0.8$, whereas A1689-217 has a $\log(\text{SFR}) = 1.2$. Furthermore, the redshift-invariant nature of the FMR and $\mu_{0.32}$ –metallicity projection only applies out to $z = 2.5$, with A1689-217 lying just beyond this redshift at $z = 2.59$. Perhaps most importantly, the Mannucci et al. (2010) FMR is defined with metallicities calculated via locally calibrated, strong-line diagnostics (Maiolino et al. 2008), the applicability of such indirect methods at high redshift being a primary focus of this paper.

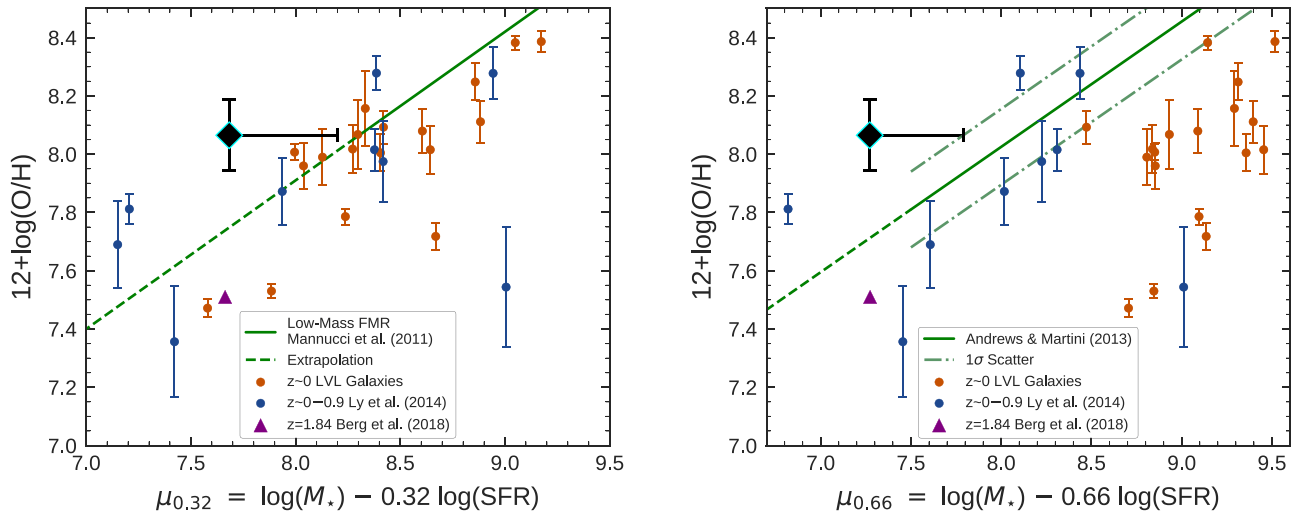


Figure 8. Left: low-mass extension of the FMR (Mannucci et al. 2010) as given by the projection of metallicity vs. μ_α (in solar units; see Equation (4)) for $\alpha = 0.32$. This extension (Equation (5)) was calculated by Mannucci et al. (2011) down to $\mu_{0.32} \sim 8.3$ (solid line), so an extrapolation in $\mu_{0.32}$ is shown here for lower values (dashed line). Right: metallicity vs. μ_α projection of the FMR as calculated by Andrews & Martini (2013). These authors report a minimization in the scatter of metallicity at fixed μ_α for $\alpha = 0.66$. This linear relation, with slope $m = 0.43$, is only calibrated down to $\mu_{0.66} \sim 7.5$ (solid line), so an extrapolation in $\mu_{0.66}$ is given here (dashed line). The scatter in the projection (based on stacks instead of individual galaxies) is given to be $\sigma = 0.13$ dex and is shown by the dotted-dashed lines. Metallicities used in Mannucci et al. (2010, 2011) are based on strong-line methods, whereas metallicities in Andrews & Martini (2013) are T_e based from stacks of SDSS spectra. In both panels, A1689-217 is given by the black diamond with cyan border. Its stellar mass of $\log(M_*/M_\odot) = 8.07$ is likely a lower limit not accounting for an undetected older stellar population (see Section 4.1 and Figure 5), so we show the increase A1689-217 would experience in μ_α for a factor of ~ 3.3 increase in stellar mass. A similar galaxy (in M_* and SFR) to A1689-217 from Brammer et al. (2012) and Berg et al. (2018) has its lower-limit metallicity (see text for details) plotted as the purple triangle. A sample of $z < 0.9$ galaxies from Ly et al. (2014) is shown in blue, and a low-mass, $z \sim 0$, LVL sample (see text for details) is shown by the dark-orange data points. All galaxy samples have their direct metallicities plotted in both panels.

Addressing the limited stellar mass range, Mannucci et al. (2011) extended the FMR, or more specifically the $\mu_{0.32}$ -metallicity projection, down to a stellar mass of $\sim 10^{8.3} M_\odot$ using ~ 1300 galaxies from the Mannucci et al. (2010) sample with $8.3 < \mu_{0.32} < 9.4$. They found that these low-mass galaxies extend the FMR with a smooth, linear relation between gas-phase metallicity and $\mu_{0.32}$ given, for $\mu_{0.32} < 9.5$, by

$$12 + \log(\text{O}/\text{H}) = 8.93 + 0.51(\mu_{0.32} - 10). \quad (5)$$

Recognizing that metallicity estimates based on different methods can differ drastically for the same galaxies (Kewley & Ellison 2008), Andrews & Martini (2013) investigated the μ_α (Equation (4)) FMR projection using the T_e -based metallicities they calculated with their stacked SDSS spectra. Using galaxies with $7.5 \lesssim \log(M_*/M_\odot) \lesssim 10.6$ and $-1.0 \leq \log(\text{SFR}) \leq 2.0$ binned by M_* and SFR, they found that $\alpha = 0.66$ minimized the scatter in their metallicities at fixed μ_α . While this calibration of the μ_α -metallicity projection utilizes direct-method oxygen abundances, it still suffers from both a lack of high-redshift data due to the faintness of T_e -sensitive auroral lines and a poor sampling of low-mass, high-SFR galaxies like A1689-217 (see Figure 1 of Andrews & Martini 2013 for the distribution in M_* and SFR of their sample).

We test the validity of the FMRs of Mannucci et al. (2011) and Andrews & Martini (2013) in the poorly sampled $M_* - \text{SFR}$ parameter space occupied by A1689-217. In Figure 8, we plot A1689-217 against the low-mass FMR extension (left) given by Equation (5), extrapolated down by ~ 0.6 dex in $\mu_{0.32}$, and against the T_e -based FMR (right), extrapolated down by ~ 0.2 dex in $\mu_{0.66}$. We also plot the $z = 1.84$ highly ionized, lensed galaxy (SL2S J02176-0513) of Brammer et al. (2012) and Berg et al. (2018), which, when adjusted for a Chabrier (2003) IMF with $0.2 Z_\odot$, has a

very similar stellar mass ($\log(M_*/M_\odot) = 8.03$) and SFR ($14 M_\odot \text{ yr}^{-1}$) to that of A1689-217. Despite these similar properties, SL2S J02176-0513 has a much lower metallicity ($12 + \log(\text{O}/\text{H}) \geq 7.51$) than A1689-217, however. We note that its metallicity is reported as a lower limit owing to both the lack of spectroscopic coverage of the $[\text{O II}] \lambda\lambda 3726, 3729$ emission lines needed for the determination of O^+/H^+ (see Equation (1)) and the possibility of a contribution from O^{+3} to O/H . Nevertheless, as detailed in Berg et al. (2018), this lower limit should be close to the actual value, as the highly ionized nature of the galaxy makes the O^+ contribution to the oxygen abundance very small (estimated at 2% of the total oxygen abundance; included in our stated lower-limit metallicity), and the ionization correction factor (ICF) for contribution of O^{+3} is also estimated to be small (ICF = 1.055; not included in our stated lower-limit metallicity).

For further comparison of A1689-217 and the FMRs to other low-mass galaxies spanning a broad range of star formation activity, we also include in Figure 8 the partial Ly et al. (2014) sample used in this work (median $\log(M_*/M_\odot) \sim 8.4$ and median $\text{sSFR} \sim 9.3 \text{ Gyr}^{-1}$) and a $z \sim 0$ LVL subsample (median $\log(M_*/M_\odot) \sim 7.7$ and median $\text{sSFR} \sim 0.2 \text{ Gyr}^{-1}$). The Ly et al. (2014) sample, in addition to using the metallicities rederived in this work, uses SFRs recalculated assuming a Cardelli et al. (1989) extinction law. Stellar masses for this sample are the values given in Ly et al. (2014) for a Chabrier (2003) IMF with $0.2 Z_\odot$. The LVL objects used here compose a subset of the Berg et al. (2012) sample used in Figures 3 and 6, of which these objects here are a part of both the sample used in Berg et al. (2012) and the sample in Weisz et al. (2012). Metallicities used here are those recalculated in this paper with the emission-line fluxes from Berg et al. (2012). Stellar masses for these galaxies are taken from Weisz et al. (2012), while the SFRs are calculated from $\text{H}\alpha$ measurements

taken by Kennicutt et al. (2008) and Lee et al. (2009) as part of the 11 Mpc $H\alpha$ and Ultraviolet Galaxy Survey (11HUGS) survey. All SFRs for A1689-217 and the comparison samples are calculated via Balmer recombination lines, assuming a Chabrier (2003) IMF with $0.2 Z_{\odot}$, and all metallicities are calculated via the “direct” method.

With the lower-limit stellar mass estimated by our SED fitting ($\log(M_*/M_{\odot}) = 8.07$), A1689-217 lies $\sim 2.6\sigma$ (2.9σ) above the extrapolation of the low-mass FMR extension of Mannucci et al. (2011) (T_e -based FMR of Andrews & Martini 2013). However, as mentioned in Section 4.1 and seen in Figure 5, an unseen, older stellar population component can exist in A1689-217 without significantly altering the observed SED, raising the stellar-mass estimate of A1689-217 by as much as a factor of 3.3 (up to $\log(M_*/M_{\odot}) = 8.59$). An increase in stellar mass will correspondingly increase the measured value of μ_{α} (Equation (4)) and bring A1689-217 into better agreement with both FMRs. This is seen in Figure 8, where the horizontal bar extending from A1689-217 represents the range of μ_{α} values corresponding to our estimated range of stellar masses for A1689-217. If the mass estimate is even $\sim 2\times$ what we state as the lower bound, A1689-217 is consistent with the FMR of Andrews & Martini (2013) within the 1σ scatter around the relation and the uncertainty in A1689-217’s oxygen abundance. Without this mass increase, A1689-217 is very likely already consistent with the extrapolation of the low-mass end of the FMR as given by Mannucci et al. (2011) considering the 1σ dispersions in metallicity seen at fixed $\mu_{0.32}$ in their work (see right panel of their Figure 1). We therefore suggest that A1689-217 is consistent with both FMRs within the observed scatter around each relation.

An important takeaway from Figure 8 is the large scatter seen around both μ_{α} -metallicity projections. This is well illustrated when comparing A1689-217 and SL2S J02176–0513 from Berg et al. (2018). Despite having similar sSFRs $\sim 135 \text{ Gyr}^{-1}$, these galaxies differ in oxygen abundance by ~ 0.55 dex, lying on either side of both FMRs. Large scatter is also seen in the Ly et al. (2014) comparison sample, despite the sample being generally consistent with both FMRs. This scatter observed in Figure 8 around the FMRs is likely due to the increased variation in star formation histories and current star formation activity in dwarf galaxies (Mannucci et al. 2011; Emami et al. 2019) and suggests that physical processes of gas flows, enrichment, and star formation have not yet reached equilibrium (Ly et al. 2015). Physical timescale effects in dwarf galaxies with bursty star formation may lead to large dispersions in the metallicities of galaxies with similar properties, like we see with A1689-217 and SL2S J02176–0513, whereby we may be observing more metal-rich galaxies at a time when recent star formation has enriched the gas but not yet removed metals from the galaxy via supernovae and other stellar feedback (Ly et al. 2015).

In consideration of the LVL sample here, we note the systematic offsets of the galaxies (median $\log(\text{SFR}) \sim -1.9$ and median $\log(M_*/M_{\odot}) \sim 7.7$) particularly from the relation of Andrews & Martini (2013), but also slightly below the relation of Mannucci et al. (2011) on average. While an in-depth study of these offsets is beyond the scope of this work, they may arise from a lack of examination of the M_* -SFR parameter space occupied by the LVL galaxies. Mannucci et al. (2011) only probe down to $M_* \sim 10^{8.3} M_{\odot}$ and $\log(\text{SFR}) \sim -1.45$, while Andrews & Martini (2013) study a sample with the

vast majority of objects having $\log(\text{SFR}) > -1$ and $\log(M_*/M_{\odot}) > 8$. The extreme offset of the LVL galaxies from the Andrews & Martini (2013) relation may also result from the stronger dependence of μ_{α} on SFR in this calibration ($\alpha = 0.66$) compared to that in Mannucci et al. (2010) ($\alpha = 0.32$).

5.5. A Comparison against the MZR Predictions of FIRE

The FIRE¹¹ simulations (Hopkins et al. 2014) are cosmological zoom-in simulations that contain realistic physical models and resolution of the multiphase structure of the ISM, star formation, and stellar feedback. Ma et al. (2016) utilize these simulations to study the evolution of the stellar mass–gas-phase metallicity relation from $z = 0$ to 6 for galaxies spanning the stellar mass range $M_* = 10^4 - 10^{11} M_{\odot}$ at $z = 0$. They predict an MZR that has a slope that does not vary appreciably with redshift. They fix the slope to the mean value with redshift, $m = 0.35$ (which almost perfectly agrees with the best-fit slope between $z = 1.4$ and $z = 3.0$; see their Figure 3), and report an MZR that evolves with z as

$$12 + \log(\text{O}/\text{H}) = 0.35[\log(M_*/M_{\odot}) - 10] + 0.93 \exp(-0.43z) + 7.95. \quad (6)$$

Comparing A1689-217 against this prediction, at $z = 2.5918$, with A1689-217’s lower-limit (upper-limit) stellar mass of $\log(M_*/M_{\odot}) = 8.07$ (8.59; see Section 4.1 and Figure 5), we find that the metallicity of A1689-217 ($12 + \log(\text{O}/\text{H}) = 8.06 \pm 0.12$) is $\sim 4.0\sigma$ (2.5σ) above the predicted oxygen abundance of $12 + \log(\text{O}/\text{H}) = 7.58$ (7.76). Comparing the prediction in Equation (6) also against the galaxy, SL2S J02176–0513, of Berg et al. (2018) at $z = 1.8444$ and $\log(M_*/M_{\odot}) = 8.03$, we find that the lower-limit metallicity of the galaxy (7.51; see Berg et al. 2018 and Section 5.4 for details on the lower limit) lies 0.17 dex below the prediction of $12 + \log(\text{O}/\text{H}) = 7.68$. Further comparing the position of both of these galaxies to the scatter around the MZR in Figure 3 of Ma et al. (2016), we see that A1689-217 lies above all simulated galaxies at its lower-limit stellar mass, but likely among the objects scattered high in oxygen abundance at its upper-limit stellar mass. SL2S J02176–0513 lies below the best-fit relation but is consistent within the scatter.

Considered together, despite being at different redshifts, these results at least show that there is significant scatter of dwarf galaxies around the MZR at roughly fixed stellar mass. This is likely due to time variations in the metallicities of dwarf galaxies resulting from the bursty nature of their star formation and its connection to gas inflows/outflows (Ma et al. 2016). Due to the extremely metal-poor nature of SL2S J02176–0513 ($\sim 0.07 Z_{\odot}$) and its general agreement with the predicted MZR, as well as the discrepancy of A1689-217 from the MZR, particularly when considering the lower end of A1689-217’s mass range, these results may also suggest that the slope ($m = 0.35$) in Equation (6) is too steep. However, larger observational samples are needed to verify this suggestion.

6. Summary

In this paper, we present a 4.2σ detection of the temperature-sensitive, auroral [O III] $\lambda 4363$ emission line in a lensed, star-forming, dwarf galaxy at $z = 2.59$, A1689-217. With the

¹¹ <https://fire.northwestern.edu/>

extinction-corrected fluxes of the rest-optical, nebular emission lines, we estimate the electron temperature and density of this galaxy and calculate, directly, an oxygen abundance of $12 + \log(\text{O}/\text{H}) = 8.06 \pm 0.12$ ($0.24 Z_{\odot}$). With this measurement and the intrinsic strong-line ratios calculated for A1689-217, we report the following:

1. We study the evolution with redshift of strong-line ratio–direct-metallicity relations calibrated and suggested to be redshift invariant out to $z \sim 0.8$ by Jones et al. (2015). With a $z \sim 0$ comparison sample from Izotov et al. (2006), the 32 $z \sim 0.8$ galaxies from Jones et al. (2015), 9 $z < 0.9$ galaxies from Ly et al. (2014), and 4 high-redshift galaxies ($z = 1.43, 1.43, 1.83, 3.08$) with [O III] $\lambda 4363$ detections in addition to A1689-217, we find no evidence for evolution of the Jones et al. strong-line ratio–metallicity calibrations. We also study the [O III]/[O II] metallicity calibration of Bian et al. (2018), the preferred metallicity diagnostic in the strong-line metallicity study of Sanders et al. (2019). We find general agreement between this relation and our samples, as well as with the relation of Jones et al. (2015). We note divergences from the Jones et al. relations of our $z \sim 0$ LVL H II region sample below $12 + \log(\text{O}/\text{H}) \sim 8.1$, similar to H II region divergences seen in Sanders et al. (2019).
2. Using the same comparison samples, we find no significant evolution with redshift in the high-excitation tail of the O_{32} versus R_{23} excitation diagram. The different galaxy samples do not display any relative offsets in either O_{32} or R_{23} , with intermediate- and high-redshift galaxies following the same distribution as local galaxies, albeit with larger scatter of the $z > 1$ sample in $\log(\text{R}_{23})$. We also observe the nearly monotonic decrease in direct metallicity with increasing O_{32} and R_{23} seen in Shapley et al. (2015). As with the strong-line ratios, we find no evidence for evolution with redshift of the metallicity as a function of position along the excitation sequence. The combination of these results supports the conclusions of Shapley et al. (2015) that the O_{32} versus R_{23} excitation diagram can be a useful, direct-metallicity-based, redshift-invariant, empirical oxygen abundance indicator.
3. Through our study of both the strong-line ratio–metallicity relations and the O_{32} versus R_{23} excitation diagram, we find no evolution with redshift of the ionization parameter at fixed O/H. This result is in agreement with Sanders et al. (2016a, 2016b, 2019), who report the same finding and suggest that the ionization state of high- z , star-forming galaxies is similar to local, metal-poor galaxies.
4. We plot A1689-217 against both the $\mu_{0.32}$ –metallicity projection of the FMR as extended to low stellar mass by Mannucci et al. (2011) and the $\mu_{0.66}$ –metallicity projection of Andrews & Martini (2013), wherein the metallicities are T_e -based as opposed to the strong-line basis of Mannucci et al. (2011). The stated stellar mass range ($\log(M_*/M_{\odot}) = 8.07\text{--}8.59$) and SFR ($16.2 M_{\odot} \text{ yr}^{-1}$) of A1689-217 yield a range in $\mu_{0.32}$ ($\mu_{0.66}$) of $\sim 7.7\text{--}8.2$ ($\sim 7.3\text{--}7.8$) and thus require slight extrapolations of both FMRs in μ_{α} (~ 0.6 dex in $\mu_{0.32}$ and ~ 0.2 dex in $\mu_{0.66}$). We also compare A1689-217 and the FMRs to other low-mass galaxy samples at low to high redshift

with a large range in current star formation activity. Together, these samples show a large scatter around the FMR, likely due to large variations in star formation history and current star formation activity in dwarf galaxies. With this observed scatter and the uncertain mass estimate of A1689-217 resulting from the possibility of the presence of an unseen, older stellar population within the galaxy, we conclude that A1689-217 is consistent with both FMRs studied.

5. We compare the locations in M_* – Z parameter space of A1689-217 and the galaxy from Berg et al. (2018) to the predicted MZR from the FIRE hydrodynamical simulations (Ma et al. 2016). A1689-217 lies $\sim 0.3\text{--}0.5$ dex above the predicted relation, while the object from Berg et al. (2018) lies ~ 0.2 dex below the relation, suggesting a large scatter in the relation at low mass and/or a slightly shallower MZR slope than predicted.

This study adds another crucial data point at high redshift in terms of direct oxygen abundance estimates and dwarf galaxy properties. With the measurements of A1689-217 and their comparisons to measurements of other auroral-line-emitting galaxies at various redshifts, we are able to further constrain the validity of several diagnostics at high redshift and low stellar mass, such as locally calibrated strong-line ratio–direct-metallicity relations and the FMR. However, large statistical samples of high-redshift [O III] $\lambda 4363$ sources and very low mass dwarf galaxies are needed to properly constrain these diagnostics. Regardless, this and other similar studies help to prepare us for those large surveys that will be conducted with the next generation of ground- and space-based telescopes.

This material is based on work supported by the National Science Foundation under grant No. 1617013.

Support for program Nos. 12201 and 12931 was provided by NASA through a grant from the Space Telescope Science Institute, which is operated by the Association of Universities for Research in Astronomy, Inc., under NASA contract NAS5-26555.

The authors wish to recognize and acknowledge the very significant cultural role and reverence that the summit of Maunakea has always had within the indigenous Hawaiian community. We are most fortunate to have the opportunity to conduct observations from this mountain.

Facilities: Keck:I (MOSFIRE, LRIS), *HST* (WFC3, ACS).

Appendix Yuan 2009 Detection

This paper includes a reanalysis of previously reported high-redshift ($z > 1$) detections of [O III] $\lambda 4363$. Yuan & Kewley (2009) reported a $\sim 3\sigma$ detection of [O III] $\lambda 4363$ in a $z = 1.7$ galaxy behind A1689, referred to as “Lens22.3” in their paper and first reported as a multiply imaged galaxy in Broadhurst et al. (2005). As part of our larger campaign to obtain near-IR spectra of lensed, high-redshift galaxies, we obtained a MOSFIRE J -band spectrum of Lens22.3 and of another image of the same galaxy (referred to as Lens22.1 in Broadhurst et al. 2005). Both images were observed in the same slit mask for 4320 s on 2015 January 20 in $\sim 0''.6$ seeing. Though our exposure time is somewhat shorter than the Yuan & Kewley (2009) observations (4320 s vs. 6800 s), the much higher spectral resolution ($R \sim 3300$ vs. $R \sim 500$) and narrower slit

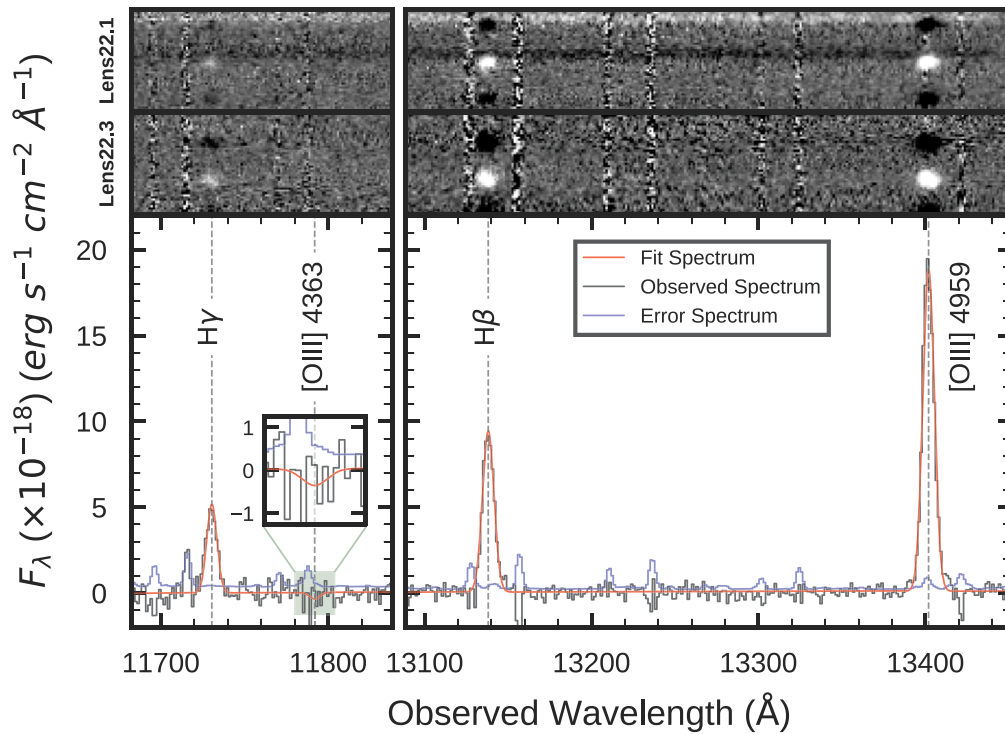


Figure 9. 2D spectra of Lens22.1 (top) and Lens22.3 (bottom) (images referred to in Broadhurst et al. 2005), two images of the same galaxy at $z = 1.7026$. Below is plotted the combined 1D spectrum of both images (black), the error spectrum (blue), and the best-fit continuum and emission lines (red). Strong emission lines are seen in $H\gamma$, $H\beta$, and $[O III] \lambda 4959$, but no detection is seen in $[O III] \lambda 4363$ (in either 1D or 2D), in disagreement with the claimed detection in Yuan & Kewley (2009). The portion of the 1D spectrum containing $[O III] \lambda 4363$ has been highlighted in green and magnified in the inset plot.

Table 3
Emission-line Fluxes of Lens22.3 and Lens22.1

Line	Relative Flux ^a	S/N
$H\gamma$	0.49	23
$[O III] \lambda 4363$	<0.03	...
$H\beta$	1.0	48
$[O III] \lambda 4959$	2.00	67

Note.

^a Fluxes relative to $H\beta$ flux.

width ($0''.7$ vs. $1''.0$) of the MOSFIRE observations result in a superior sensitivity to narrow emission lines. For a specific comparison in the J band, our detections of $H\beta$ are 35σ and 28σ for Lens22.3 and Lens22.1, respectively, compared to 5σ for the Yuan & Kewley (2009) detection. For additional sensitivity to faint lines, we normalized the two spectra (by the $[O III] \lambda 4959$ flux) and created a weighted-average spectrum, resulting in an $H\beta$ detection of 48σ .

The 2D spectra of Lens22.3 and Lens22.1 and the stacked 1D spectrum can be seen in Figure 9. Strong $[O III] \lambda 4959$, $H\beta$, and a 23σ detection of $H\gamma$ can be seen. However, there is no evidence of an $[O III] \lambda 4363$ line. Our stacked flux values and 1σ upper limit flux of $[O III] \lambda 4363$, all relative to $H\beta$, are presented in Table 3. Given the reported $H\beta/[O III] \lambda 4363 \sim 3.7$, we should have detected the line at $\sim 9.2\sigma$. Given the much lower spectral resolution of the Subaru/MOIRCS spectrum of Yuan & Kewley (2009), we believe that the line detected in the MOIRCS spectrum was likely the $H\gamma$ line. That would also help explain why the line center reported in that spectrum was at a somewhat lower redshift than the other lines ($z = 1.696$ vs. $z = 1.705$).

A more detailed analysis of this spectrum and the rest of our sample will be reported in future works.

ORCID iDs

Timothy Gburek <https://orcid.org/0000-0002-7732-9205>
 Brian Siana <https://orcid.org/0000-0002-4935-9511>
 Anahita Alavi <https://orcid.org/0000-0002-8630-6435>
 Najmeh Emami <https://orcid.org/0000-0003-2047-1689>
 Johan Richard <https://orcid.org/0000-0001-5492-1049>
 William R. Freeman <https://orcid.org/0000-0003-3559-5270>

References

- Abazajian, K., Adelman-McCarthy, J. K., Agüeros, M. A., et al. 2005, *AJ*, **129**, 1755
 Abazajian, K. N., Adelman-McCarthy, J. K., Agüeros, M. A., et al. 2009, *ApJS*, **182**, 543
 Alavi, A., Siana, B., Richard, J., et al. 2014, *ApJ*, **780**, 143
 Alavi, A., Siana, B., Richard, J., et al. 2016, *ApJ*, **832**, 56
 Alloin, D., Collin-Souffrin, S., Joly, M., & Vigroux, L. 1979, *A&A*, **78**, 200
 Andrews, B. H., & Martini, P. 2013, *ApJ*, **765**, 140
 Asplund, M., Grevesse, N., Sauval, A. J., & Scott, P. 2009, *ARA&A*, **47**, 481
 Atek, H., Kneib, J.-P., Pacifici, C., et al. 2014, *ApJ*, **789**, 96
 Atek, H., Siana, B., Scarlata, C., et al. 2011, *ApJ*, **743**, 121
 Baldwin, J. A., Phillips, M. M., & Terlevich, R. 1981, *PASP*, **93**, 5
 Berg, D. A., Erb, D. K., Auger, M. W., Pettini, M., & Brammer, G. B. 2018, *ApJ*, **859**, 164
 Berg, D. A., Skillman, E. D., Marble, A. R., et al. 2012, *ApJ*, **754**, 98
 Bian, F., Kewley, L. J., & Dopita, M. A. 2018, *ApJ*, **859**, 175
 Brammer, G. B., Sánchez-Janssen, R., Labbé, I., et al. 2012, *ApJL*, **758**, L17
 Brinchmann, J., Pettini, M., & Charlot, S. 2008, *MNRAS*, **385**, 769
 Broadhurst, T., Benítez, N., Coe, D., et al. 2005, *ApJ*, **621**, 53
 Bruzual, G., & Charlot, S. 2003, *MNRAS*, **344**, 1000
 Campbell, A., Terlevich, R., & Melnick, J. 1986, *MNRAS*, **223**, 811
 Cardelli, J. A., Clayton, G. C., & Mathis, J. S. 1989, *ApJ*, **345**, 245
 Chabrier, G. 2003, *PASP*, **115**, 763

- Charlot, S., & Fall, S. M. 2000, *ApJ*, **539**, 718
- Christensen, L., Laursen, P., Richard, J., et al. 2012, *MNRAS*, **427**, 1973
- Cullen, F., Cirasuolo, M., Kewley, L. J., et al. 2016, *MNRAS*, **460**, 3002
- Dale, D. A., Cohen, S. A., Johnson, L. C., et al. 2009, *ApJ*, **703**, 517
- Davis, M., Faber, S. M., Newman, J., et al. 2003, *Proc. SPIE*, **4834**, 161
- Denicoló, G., Terlevich, R., & Terlevich, E. 2002, *MNRAS*, **330**, 69
- Dopita, M. A., & Sutherland, R. S. 2003, *Astrophysics of the Diffuse Universe* (Berlin: Springer)
- Dopita, M. A., Sutherland, R. S., Nicholls, D. C., Kewley, L. J., & Vogt, F. P. A. 2013, *ApJS*, **208**, 10
- Eldridge, J. J., & Stanway, E. R. 2009, *MNRAS*, **400**, 1019
- Emami, N., Siana, B., Weisz, D. R., et al. 2019, *ApJ*, **881**, 71
- Erb, D. K., Shapley, A. E., Pettini, M., et al. 2006, *ApJ*, **644**, 813
- Foreman-Mackey, D., Hogg, D. W., Lang, D., & Goodman, J. 2013, *PASP*, **125**, 306
- Freeman, W. R., Siana, B., Kriek, M., et al. 2019, *ApJ*, **873**, 102
- Gordon, K. D., Clayton, G. C., Misselt, K. A., Landolt, A. U., & Wolff, M. J. 2003, *ApJ*, **594**, 279
- Henry, A., Scarlata, C., Domínguez, A., et al. 2013, *ApJL*, **776**, L27
- Hirschmann, M., Charlot, S., Feltre, A., et al. 2017, *MNRAS*, **472**, 2468
- Hopkins, P. F., Kereš, D., Oñorbe, J., et al. 2014, *MNRAS*, **445**, 581
- Izotov, Y. I., Stasińska, G., Meynet, G., Guseva, N. G., & Thuan, T. X. 2006, *A&A*, **448**, 955
- James, B. L., Pettini, M., Christensen, L., et al. 2014, *MNRAS*, **440**, 1794
- Jensen, E. B., Strom, K. M., & Strom, S. E. 1976, *ApJ*, **209**, 748
- Jones, T., Martin, C., & Cooper, M. C. 2015, *ApJ*, **813**, 126
- Kashikawa, N., Shimasaku, K., Yasuda, N., et al. 2004, *PASJ*, **56**, 1011
- Kashino, D., Silverman, J. D., Sanders, D., et al. 2017, *ApJ*, **835**, 88
- Kauffmann, G., Heckman, T. M., Tremonti, C., et al. 2003, *MNRAS*, **346**, 1055
- Kelson, D. D. 2003, *PASP*, **115**, 688
- Kennicutt, R. C. Jr. 1998, *ARA&A*, **36**, 189
- Kennicutt, R. C. Jr., Lee, J. C., Funes, J. G., et al. 2008, *ApJS*, **178**, 247
- Kewley, L. J., & Dopita, M. A. 2002, *ApJS*, **142**, 35
- Kewley, L. J., Dopita, M. A., Leitherer, C., et al. 2013, *ApJ*, **774**, 100
- Kewley, L. J., Dopita, M. A., Sutherland, R. S., Heisler, C. A., & Trevena, J. 2001, *ApJ*, **556**, 121
- Kewley, L. J., & Ellison, S. L. 2008, *ApJ*, **681**, 1183
- Kewley, L. J., Zahid, H. J., Geller, M. J., et al. 2015, *ApJL*, **812**, L20
- Kriek, M., Shapley, A. E., Reddy, N. A., et al. 2015, *ApJS*, **218**, 15
- Kriek, M., van Dokkum, P. G., Labbé, I., et al. 2009, *ApJ*, **700**, 221
- Lara-López, M. A., Cepa, J., Bongiovanni, A., et al. 2010, *A&A*, **521**, L53
- Lee, J. C., Gil de Paz, A., Tremonti, C., et al. 2009, *ApJ*, **706**, 599
- Ly, C., Malkan, M. A., Nagao, T., et al. 2014, *ApJ*, **780**, 122
- Ly, C., Rigby, J. R., Cooper, M., & Yan, R. 2015, *ApJ*, **805**, 45
- Ma, X., Hopkins, P. F., Faucher-Giguère, C.-A., et al. 2016, *MNRAS*, **456**, 2140
- Maiolino, R., & Mannucci, F. 2019, *A&ARv*, **27**, 3
- Maiolino, R., Nagao, T., Grazian, A., et al. 2008, *A&A*, **488**, 463
- Mannucci, F., Cresci, G., Maiolino, R., Marconi, A., & Gnerucci, A. 2010, *MNRAS*, **408**, 2115
- Mannucci, F., Salvaterra, R., & Campisi, M. A. 2011, *MNRAS*, **414**, 1263
- Maseda, M. V., van der Wel, A., Rix, H.-W., et al. 2014, *ApJ*, **791**, 17
- Masters, D., McCarthy, P., Siana, B., et al. 2014, *ApJ*, **785**, 153
- McGaugh, S. S. 1991, *ApJ*, **380**, 140
- McLean, I. S., Steidel, C. C., Epps, H., et al. 2010, *Proc. SPIE*, **7735**, 77351E
- McLean, I. S., Steidel, C. C., Epps, H. W., et al. 2012, *Proc. SPIE*, **8446**, 84460J
- Nakajima, K., & Ouchi, M. 2014, *MNRAS*, **442**, 900
- Nakajima, K., Ouchi, M., Shimasaku, K., et al. 2013, *ApJ*, **769**, 3
- Newman, J. A., Cooper, M. C., Davis, M., et al. 2013, *ApJS*, **208**, 5
- Oke, J. B., Cohen, J. G., Carr, M., et al. 1995, *PASP*, **107**, 375
- Onodera, M., Carollo, C. M., Lilly, S., et al. 2016, *ApJ*, **822**, 42
- Osterbrock, D. E., & Ferland, G. J. 2006, *Astrophysics of Gaseous Nebulae and Active Galactic Nuclei* (Sausalito, CA: Univ. Science Books)
- Pagel, B. E. J., Edmunds, M. G., Blackwell, D. E., Chun, M. S., & Smith, G. 1979, *MNRAS*, **189**, 95
- Patrício, V., Christensen, L., Rhodin, H., Cañameras, R., & Lara-López, M. A. 2018, *MNRAS*, **481**, 3520
- Pettini, M., & Pagel, B. E. J. 2004, *MNRAS*, **348**, L59
- Pilyugin, L. S., & Thuan, T. X. 2005, *ApJ*, **631**, 231
- Reddy, N. A., Oesch, P. A., Bouwens, R. J., et al. 2018, *ApJ*, **853**, 56
- Sanders, R. L., Shapley, A. E., Kriek, M., et al. 2015, *ApJ*, **799**, 138
- Sanders, R. L., Shapley, A. E., Kriek, M., et al. 2016a, *ApJ*, **816**, 23
- Sanders, R. L., Shapley, A. E., Kriek, M., et al. 2016b, *ApJL*, **825**, L23
- Sanders, R. L., Shapley, A. E., Reddy, N. A., et al. 2019, arXiv:1907.00013
- Shapley, A. E., Reddy, N. A., Kriek, M., et al. 2015, *ApJ*, **801**, 88
- Shaw, R. A., & Dufour, R. J. 1994, in ASP Conf. Ser. 61, *Astronomical Data Analysis Software and Systems III*, ed. D. R. Crabtree, R. J. Hanisch, & J. Barnes (San Francisco, CA: ASP), 327
- Shirazi, M., Brinchmann, J., & Rahmati, A. 2014, *ApJ*, **787**, 120
- Stark, D. P., Auger, M., Belokurov, V., et al. 2013, *MNRAS*, **436**, 1040
- Steidel, C. C., Rudie, G. C., Strom, A. L., et al. 2014, *ApJ*, **795**, 165
- Steidel, C. C., Shapley, A. E., Pettini, M., et al. 2004, *ApJ*, **604**, 534
- Storchi-Bergmann, T., Calzetti, D., & Kinney, A. L. 1994, *ApJ*, **429**, 572
- Storey, P. J., & Zeippen, C. J. 2000, *MNRAS*, **312**, 813
- Straughn, A. N., Kuntschner, H., Kümmel, M., et al. 2011, *AJ*, **141**, 14
- Strom, A. L., Steidel, C. C., Rudie, G. C., et al. 2017, *ApJ*, **836**, 164
- Strom, A. L., Steidel, C. C., Rudie, G. C., Trainor, R. F., & Pettini, M. 2018, *ApJ*, **868**, 117
- Tang, M., Stark, D., Chevallard, J., & Charlot, S. 2019, *MNRAS*, **489**, 2572
- Tremonti, C. A., Heckman, T. M., Kauffmann, G., et al. 2004, *ApJ*, **613**, 898
- Troncoso, P., Maiolino, R., Sommariva, V., et al. 2014, *A&A*, **563**, A58
- van der Wel, A., Straughn, A. N., Rix, H. W., et al. 2011, *ApJ*, **742**, 111
- Weisz, D. R., Johnson, B. D., Johnson, L. C., et al. 2012, *ApJ*, **744**, 44
- Yuan, T. T., & Kewley, L. J. 2009, *ApJL*, **699**, L161
- Zahid, H. J., Geller, M. J., Kewley, L. J., et al. 2013, *ApJL*, **771**, L19